

Marine Heatwaves across the central South Pacific: characteristics, mechanisms, and modulation by El Niño Southern Oscillation

Bastien Pagli^{1,6}, Takeshi Izumo¹, Alexandre Barboni², Carla Chevillard³, Cyril Dutheil⁴, Raphaël Legrand⁵, Christophe Menkes⁶, Claire Rocuet¹ and Sophie Cravatte⁷

¹UMR 241 SECOPOL, (IRD, ILM, Ifremer, UPF), Tahiti, French Polynesia

²Laboratoire d'Etudes en Géophysique et Océanographie Spatiales (LEGOS), Toulouse, France

³IFREMER, Tahiti, French Polynesia

⁴MARBEC, University of Montpellier, CNRS, Ifremer, IRD, Sète, France

⁵DIRPF, Météo France, Tahiti, French Polynesia

⁶ENTROPIE (IRD, Ifremer, Université de la Réunion, Université de la Nouvelle-Calédonie), Nouméa, New Caledonia

⁷Université de Toulouse, LEGOS (IRD, CNES, CNRS, UT3), Toulouse, France.

Correspondence to: Bastien Pagli (bastien.pagli@ird.fr)

Abstract. Marine heatwaves (MHWs) are intensifying with climate change, endangering ecosystems such as coral reefs. Yet their regional characteristics and drivers remain poorly understood in many parts of the Pacific. Here we provide a comprehensive assessment of MHWs in the central South Pacific and across the five archipelagos of French Polynesia (FP; representing more than 5 million km² of maritime area, a region as vast as Europe), using sea surface temperature observations and an ocean reanalysis to investigate underlying mechanisms. MHW characteristics vary widely across the region: its northern and southern parts (the Marquesas and Austral archipelagos respectively) experience the highest number of MHW days and the strongest cumulative intensities, especially during the warm season (Nov-Apr). In contrast, its central part (the Society, Tuamotu, and Gambier Islands) exhibits more moderate MHW characteristics. Heat budget analyses highlight the seasonally and regionally diverse mechanisms shaping MHWs. In central FP during the warm season, (austral summer), most MHWs are driven by air-sea heat fluxes, while in the northern part, those driven by oceanic horizontal advection dominate. During the cold season, (austral winter), more MHWs driven by horizontal advection are observed in the whole region since the thicker seasonal mixed layer reduces the proportion of MHWs driven by air-sea fluxes. El Niño-Southern Oscillation (ENSO) strongly modulates MHW occurrences: El Niño favors MHW occurrences in northeastern FP, while La Niña increases MHW occurrence in the southwest with different spatial extent depending on ENSO flavors (Central or Eastern Pacific ENSO events). This modulation arises from reduced wind-evaporation cooling with reduced wind speed, shoaled mixed layers, and enhanced horizontal heat advection, occurring primarily to the northeast of French Polynesia during El Niño and to the southwest during La Niña. These results greatly improve our understanding of MHW characteristics, dynamics and variability in this ecologically-fragile region.

a supprimé: the

a supprimé: B.

a supprimé: T.

a supprimé: A.

a supprimé: C.

a supprimé: C.

a supprimé: R.

a mis en forme : Français, Exposant

a mis en forme : Français

a mis en forme : Français

a supprimé: C.

a supprimé: C.

a supprimé: S.

a mis en forme : Français

a mis en forme : Français

a mis en forme : Français

a mis en forme : Français

a supprimé: ~77 atolls, more than half of world's atolls, and

a supprimé: exposure varies

a supprimé: .

a supprimé: of

a supprimé: .

a supprimé: reduce

a supprimé: MHWs occurrence

a supprimé: MHWs occurrence

a supprimé: across

a supprimé: and

a supprimé: .

a mis en forme : Anglais (E.U.)

54 1- Introduction

55 Extreme ocean temperature, persisting in time, known as marine heatwaves (MHWs), have significant impacts on marine
56 ecosystems and, consequently, on island communities that rely on ecosystem services, fisheries, and tourism. Their
57 frequency and duration have increased over recent decades due to global ocean warming and are projected to continue rising
58 in the future (Oliver et al., 2018, 2019). Developing skillful forecasts of MHWs is therefore essential ~~to anticipate~~ their
59 impacts and, in turn, support effective mitigation. Such forecasts depend on a robust understanding of MHW characteristics,
60 their mechanisms, their physical drivers, and their variability (Holbrook et al., 2020). None of these aspects has yet been
61 studied in detail over the French Polynesia (FP) region where MHWs can lead to severe socioeconomic
62 consequences (Hédouin et al., 2020).

63 Some initial results regarding the mean characteristics and the dominant climate modes driving MHWs over FP can be
64 extracted from past studies conducted at broader spatial scales, such as the South Pacific or even globally. In the South-
65 Central Pacific, El Niño Southern Oscillation (ENSO) with its different phases El Niño (EN) and La Niña (LN) is known to
66 be an important driver of increased and suppressed MHW occurrence (Holbrook et al., 2019, 2022) and MHW intensity (Sen
67 Gupta et al., 2020). Additionally, the different flavors of ENSO (Capotondi et al., 2020) exhibit distinct connections with
68 MHWs across the Pacific Ocean in terms of both intensity and frequency. Using Linear Inverse Model (LIM) data, Gregory
69 et al., (2024) showed that these relationships vary between the Eastern Pacific (EP) and Central Pacific (CP) flavors of EN
70 and LN. In the tropical Pacific, both MHW intensity and occurrence tend to be consistent with sea surface temperature (SST)
71 anomalies during ENSO events, with maxima occurring in the central Pacific during CP EN events and in the eastern Pacific
72 during EP EN events.

73 Regarding the mechanisms of MHWs, global studies generally rely on numerical models to estimate the main physical
74 processes driving MHWs globally (Marin et al., 2022; Vogt et al., 2022; Bian et al., 2023, 2024). These studies aim at
75 identifying the dominant mechanisms during MHWs among oceanic heat advection, air/sea heat flux, horizontal and vertical
76 mixing and entrainment at the mixed layer base depending on the methods used to calculate mixed layer heat budgets during
77 MHWs. The dominant mechanisms during the MHWs' onset and decay are region dependent (Elzahaby et al., 2022; Bian et
78 al., 2023) and also depend on the spatial resolution of the model, which controls its ability to resolve oceanic eddies (Bian et
79 al., 2024). This highlights the need for regional studies and observation-based studies to better understand MHWs (e.g.
80 Schlegel et al., 2021; Elzahaby et al., 2021; Dutheil et al., 2024; Lal et al., 2025).

81 In austral summer (from November to April), which is the time of the year where ENSO events generally reach their peak of
82 intensity, ENSO strongly modifies SST, ocean currents, precipitation, and wind over FP compared to climatology. Opposite
83 influences across different parts of the country are observed depending on the ENSO flavor, due to FP's geographical
84 position near the transition zone where ENSO SST anomalies change sign and ENSO non-linear effect on the South Pacific
85 Convergence Zone (SPCZ) position (Vincent et al., 2011; Pagli et al., 2025a). EN (LN) events typically warm (cool) the
86 northeastern half of FP while cooling (warming) the southwestern half, though the boundaries and intensity of these

a supprimé: Marine heatwaves (MHWs), known as prolonged periods of Extreme ocean temperature,

a supprimé: ,

a supprimé: for mitigating

a mis en forme : Anglais (G.B.)

a mis en forme : Anglais (G.B.)

a mis en forme : Anglais (G.B.)

a supprimé: .

a supprimé: the

a supprimé: are

a supprimé: drivers

a mis en forme : Anglais (E.U.)

a supprimé: likelihood

a mis en forme : Anglais (E.U.)

a supprimé: MHWs

a supprimé: model

a supprimé: dependent due

a supprimé: the resolution or not of

a supprimé: by the model

a mis en forme : Anglais (G.B.)

a mis en forme : Anglais (G.B.)

a mis en forme : Anglais (G.B.)

a mis en forme : Anglais (G.B.)

a mis en forme : Anglais (E.U.)

a supprimé: impacts

a supprimé: FP

a supprimé: often close to

a supprimé: edges

a supprimé: its

a mis en forme : Anglais (G.B.)

106 anomalies vary by ENSO flavor. During extreme EP EN events, a strong northeastward migration of the SPCZ (Vincent et
107 al., 2011) induces enhanced precipitation and cloud cover in the northern half of FP, with intensified westerly wind
108 anomalies. This increases Ekman pumping which deepens the thermocline in the northeastern half of FP and results in a
109 weakening of the westward-flowing South Equatorial Current (SEC) and a strengthening of the South Equatorial
110 Countercurrent (SECC) (Martinez et al., 2009). In contrast, CP EN events cause a more moderate northeastward SPCZ shift
111 relative to its mean position and weaker surface winds over central FP. Moderate-to-strong LN events shift the SPCZ
112 southwest, reducing cloud cover and enhancing trade winds, strengthening the SEC and weakening the SECC. These
113 changes are amplified during very strong LN episodes (Pagli et al., 2025a). Overall, ENSO modulates surface ocean and
114 atmospheric conditions, altering the large-scale background state in which MHWs may develop.

115 The aim of this study is to analyze in detail past oceanic MHWs over FP in order to address the following questions: What
116 are the characteristics of past MHWs over FP and across the archipelagos? To what extent does ENSO drive, or modulate
117 these extreme events and their dynamics? What are the local mechanisms responsible for the onset/ decay of these events
118 across the area?

119 Section 2 describes the data and methods used to address these questions. Section 3 presents the characteristics of past
120 MHWs over FP, while section 4 explores their modulation by ENSO. Section 5 investigates the underlying mechanisms
121 driving these MHWs, and sections 6 and 7 provide the discussion and conclusions.

122

123 2- Data and Methods

124 2.1-Data and reanalysis data

125 Daily SST data were obtained from the Optimum Interpolation Sea Surface Temperature version 2 (OISSTv2) dataset, a
126 blend of in situ and satellite observations (Huang et al., 2021), covering the period from 1981 (01 Sept) to 2024 (31 Dec) on
127 a 0.25° grid. The mechanisms driving the MHWs detected over FP were investigated using the global eddy-resolving 1/12°
128 ocean reanalysis GLORYS12v1 (Lellouche et al., 2021), hereafter named GLORYS. In GLORYS the ocean and sea ice
129 general circulation model is NEMO (Madec et al., 2024). Daily oceanic variables—including potential temperature, mixed
130 layer depth, zonal and meridional currents—were analyzed. In addition, surface heat and momentum fluxes used to force the
131 oceanic model were analyzed. GLORYS reanalysis is forced by ERA-Interim until 2019 (Dee et al., 2011) and ERA5
132 afterwards (Hersbach et al., 2020). Due to the known large biases in radiative fluxes at the surface in ERA-Interim, large-
133 scale corrections were made using the NASA/GEWEX Surface Radiation Budget 3.0/3.1 product (Stackhouse et al., 2021)
134 for shortwave and longwave fluxes (Lellouche et al., 2021). Along track altimeter sea-level anomaly, satellite sea surface
135 temperature (AVHRR SST from NOAA) and sea-ice concentration (Ifremer/CERSAT) as well as in situ temperature and
136 salinity vertical profiles (CORA database from CMEMS) are assimilated in GLORYS. Tides are not represented explicitly in

a supprimé: impacts

a supprimé: and

a supprimé: depth, weakens

a supprimé: strengthens

a mis en forme : Anglais (E.U.)

a mis en forme : Anglais (E.U.)

a supprimé: and discussion

a supprimé: model simulations

a supprimé: OISSTv2

a supprimé: resolution

a supprimé: (including the large-scale corrections applied by Lellouche et al., 2021), ...

147 GLORYS (Lellouche et al., 2018). Because of data assimilation, the heat and momentum budgets are not closed in GLORYS
 148 but previous studies showed its realism for analyzing MHW heat budget in the South Pacific (Dutheil et al., 2024).
 149 MHW detection was performed using both OISSTv2 (from 1981 to 2024) and GLORYS (from 1993 to 2024). However, the
 150 mixed layer heat budget in GLORYS (see Methods) was limited to the period from 1993 to 2020 due to the forcing fields
 151 (momentum and heat fluxes) data availability. For consistency with the OISST results, GLORYS fields were regridded onto
 152 the spatial grid of the OISST dataset at 0.25° using a first order conservative remapping method.

153

154 2.2-Methods

155 MHW detection

156 MHWs were detected in the OISSTv2 dataset, and independently in the GLORYS reanalysis over the FP domain (165°W–
 157 130°W, 30°S–0°S) for the period 1981–2024 (respectively 1993–2024), following the method described by Hobday et al.,
 158 (2016). For each product, we used the 1993–2020 period as the climatological baseline. At each grid point, a MHW was
 159 identified when daily SST exceeded the 90th seasonally varying percentile (SST^{90th}) (cf. Fig. S1 for [austral summer](#) and
 160 [winter](#) average of the threshold over FP) for at least five consecutive days. SST^{90th} was computed with a moving 11-day
 161 window to ensure enough daily SST samples for a robust 90th-percentile estimate. A 31-day [moving window](#) was then
 162 applied to remove high-frequency noise. The same filter was used for the SST climatology. Events separated by [less](#) than
 163 two days were considered as a single continuous event. Standard metrics were then calculated for each MHW, following the
 164 methodology of Hobday et al. (2016). These [included the maximum, mean, and cumulative intensity, duration, onset and](#)
 165 [decline rates \(defined as the mean SST rate of change from start to peak and from peak to end, respectively\). The number of](#)
 166 [events](#) and the gaps between events [were also computed](#). MHW intensity was expressed either in absolute terms (i.e., the
 167 actual SST) or relative to the mean climatological baseline. MHWs were detected independently at each grid point; no
 168 spatial connectivity was assumed between neighboring points. [Then the](#) daily analysis of MHW occurrence across the
 169 domain was conducted to identify connected MHW areas (Lal et al., 2025). At each daily timestep, connected MHW pixels
 170 were labeled, and the area of each labeled object was calculated. For each pointwise-detected MHW, the mean and
 171 maximum spatial extent of the labeled object it belonged to were calculated over the event’s duration. [Throughout the](#)
 172 [manuscript](#), a distinction was made between MHWs occurring during the austral winter ([referred to as “cold season”](#)) and
 173 those occurring during the austral summer ([referred to as “warm season”](#)), according to the date of their peak intensity.

174 The severity index (S) introduced by Sen Gupta et al., (2020) was also computed on a daily basis in OISSTv2:

$$Severity\ Index\ (S) = \frac{SST - SST_{clim}}{SST^{90th} - SST_{clim}} \quad (1)$$

175

176 where SST_{clim} is the SST climatology. $S > 1$ indicates that SST exceeds the 90th percentile (i.e., $SST > SST^{90th}$), while $0 < S$
 177 < 1 reflects SST values warmer than the seasonal average but not exceeding the threshold. Conversely, $S < 0$ denotes [SST](#)

a supprimé: warm

a mis en forme : Anglais (E.U.)

a supprimé: cold seasons

a supprimé: were

a supprimé: smoothing filter

a supprimé: has been

a supprimé: fewer

a supprimé: include

a supprimé: number of events,

a mis en forme : Anglais (E.U.)

a mis en forme : Anglais (E.U.)

a supprimé:),

a supprimé: .

a supprimé: can be

a mis en forme : Anglais (E.U.)

a supprimé: Nevertheless, a

a supprimé: In

a mis en forme : Anglais (E.U.)

a supprimé: various sections

a supprimé: is

a mis en forme : Anglais (E.U.)

a supprimé: .

194 cooler than climatology. The severity of MHWs is generally described by values of S (Hobday et al., 2018). A MHW is
 195 categorized as moderate ($1 < S \leq 2$), strong ($2 < S \leq 3$), severe ($3 < S \leq 4$) or extreme ($S \geq 4$).
 196

197 In order to quantify the variability of the cumulative heat stress felt by the marine ecosystems, the daily Degree-Heating
 198 Weeks (DHW), commonly employed in coral bleaching risk assessments, were computed for each austral summer from
 199 1981 to 2024 following Skirving et al., (2020). First, daily temperature anomalies (HotSpot) were computed relative to the
 200 local Maximum of Monthly Mean (MMM), defined as the climatological maximum of monthly mean temperatures
 201 computed over the baseline period. DHW on each day were then estimated by summing the daily HotSpot anomalies
 202 exceeding 1 °C over the preceding 12 weeks (84 days). This accumulated value was divided by seven to express DHW in
 203 °C-weeks.

204 Results were presented as averaged for the entire FP domain, and for each of the five main archipelagos: the Marquesas,
 205 Tuamotu, Society, Gambier, and Austral Islands. The regions associated with each archipelago, over which MHW metrics
 206 were aggregated, were defined using the official administrative geographic dataset for FP provided by the French
 207 government (datagouv; see references).

208 Removing a long term temperature trend (shown in Fig. S2 for FP region) before applying the detection method is a
 209 methodological choice, as is the selection of a fixed versus a shifting baseline, both of which can influence the results and
 210 their significance (Amaya et al., 2023; Sen Gupta, 2023; Capotondi et al., 2024; Smith et al., 2025). A central question
 211 underlying these methodological choices is the definition of the “normal” state against which extreme ocean temperatures
 212 are identified. This ambiguity complicates both the definition of MHWs and the communication of MHW-related risks to the
 213 public. As a result, considerable discussion has emerged regarding MHW naming conventions and definition (Amaya et al.,
 214 2023, Sen Gupta, 2023, Smith et al., 2025). While some disagreement persists in the community regarding the definition of a
 215 MHW, it appears that both approaches are complementary, and the most appropriate depends on the specific research
 216 question to address (Smith et al., 2025). Here, we followed the guidance of Smith et al. (2025) by explicitly distinguishing
 217 MHW events identified using each approach and by clearly stating the motivation underlying the results presented. In the
 218 context of a fixed-baseline framework, retaining the long-term trend is particularly appropriate when assessing the impacts
 219 of MHWs on ecosystems or organisms with limited adaptive capacity. Conversely, when the focus is on interannual
 220 variability, climate mode relationships, or the physical mechanisms driving MHWs, removing the trend can be advantageous
 221 for isolating these signals from the longer-term climate trends. For these reasons, the section that describes the MHWs
 222 metrics over FP was made without removing the trend (section 3) and the sections analyzing the link with ENSO and the
 223 mechanisms of MHW was made with detrended SST data (section 4-5). For section 3, complementary results based on
 224 detrended SST data—where the MHW detection method and threshold computation were reapplied—are provided in the
 225 Supplementary Information (SI). Briefly, detrending does not alter the main results — such as differences between
 226 archipelagos, ENSO modulation, dominant mechanisms — but does slightly affect some quantitative MHW characteristics,
 227 including their duration, intensity, and onset/decline rates.

- a supprimé: -
- a supprimé: -average SST
- a mis en forme : Anglais (E.U.)
- a mis en forme : Anglais (E.U.)
- a supprimé:)
- a mis en forme : Anglais (E.U.)
- a supprimé: based on .
- a mis en forme : Anglais (G.B.)
- a supprimé: Whether or not
- a mis en forme : Anglais (E.U.)
- a supprimé: .
- a mis en forme : Anglais (E.U.)
- a supprimé: .
- a mis en forme : Anglais (E.U.)
- a supprimé: . Retaining the
- a supprimé: ., and estimating the “total heat exposure”, is more suitable is particularly appropriate
- a mis en forme : Anglais (G.B.)
- a mis en forme : Anglais (G.B.)
- a supprimé: human societies and marine ecosystems, as it r (... [1])
- a supprimé: investigating
- a mis en forme (... [2])
- a mis en forme (... [3])
- a supprimé: links with
- a supprimé: modes
- a supprimé: underlying
- a supprimé: useful to better isolate
- a mis en forme (... [4])
- a mis en forme (... [5])
- a mis en forme (... [6])
- a supprimé: .
- a supprimé: this reason
- a supprimé: part
- a mis en forme (... [7])
- a mis en forme (... [8])
- a supprimé: part
- a mis en forme (... [9])
- a supprimé:
- a mis en forme (... [10])

252

253 **MHW/ENSO relationships**

254 The link between MHWs and ENSO was examined at two levels of complexity. First, MHW occurrence across FP in all
 255 seasons was analyzed separately for EN, LN, and **Neutral (N)** phases, based on the Oceanic Niño Index (ONI; NOAA), using
 256 the criterion that EN (respectively LN) conditions corresponded to $ONI > 0.5$ (*resp.* < -0.5) for at least five consecutive
 257 months (see Fig. S3 for the different periods considered as EN and LN). Second, ENSO diversity was considered using the
 258 FP-specific classification developed by Pagli et al. (2025a). This classification identified six ENSO clusters based on
 259 interannual relative SST anomalies, precipitation (PR), and 850 hPa zonal wind (U850) averaged over the austral summer:
 260 three EN types (Extreme EP, Strong Mixed, and CP), one **group (EPLN+N) gathering Neutral (N) and weak EP LN group**
 261 (EPLN+N), and two LN types (CP and Strong Mixed). The classified years are presented in Table S1 (including the 2023-
 262 2024 **Strong Mixed EN event**, cf. Pagli et al. 2025b). For this classification, the analysis of MHW–ENSO relationships was
 263 restricted to the austral summer. MHW characteristics were composited for each of the six ENSO groups. For each ENSO
 264 cluster, both the S index and percentage of days with $S \geq 1$ were computed over the FP domain. The maximum of DHW
 265 reached over the warm season was also computed each year and composited by ENSO clusters.

266

267 **Mixed layer heat budget and MHW category**

268 The mechanisms of MHWs were investigated through a mixed layer heat budget analysis performed in GLORYS based on
 269 the following equation (Moisan and Niiler, 1998; Oliver et al., 2021; Dutheil et al., 2024):

$$\underbrace{\frac{\partial \langle T \rangle'}{\partial t}}_{\text{tendency}} = \underbrace{-\langle \mathbf{U} \rangle \cdot \nabla \langle T \rangle'}_{\text{Horizontal advection HADV}} + \underbrace{\left(\frac{Q_{net}}{\rho c_p h} \right)'}_{\text{Air-sea heat flux } Q} + \underbrace{Residual'}_{RES} \quad (2)$$

270

271 with

$$Residual = \underbrace{\langle \nabla \cdot (\kappa_h \nabla T) \rangle}_{\text{Horizontal mixing}} - \underbrace{\frac{1}{h} \kappa_z \frac{\partial T}{\partial z}}_{\text{Vertical mixing}} - \underbrace{\left(\frac{\langle T \rangle - T_{-h}}{h} \right) \left(\frac{\partial h}{\partial t} + \mathbf{U}_{-h} \cdot \nabla h + w_{-h} \right)}_{\text{Entrainment}} + \underbrace{\frac{DA}{Data \text{ assimilation increments}}}_{\text{Data assimilation increments}} \quad (3)$$

272

273 where $\rho = 1027 \text{ kg/m}^3$ is the mean density of sea water, $c_p = 4187 \text{ J} \cdot \text{K}^{-1} \cdot \text{kg}^{-1}$ is the specific heat capacity of seawater, κ_h
 274 and κ_z are the horizontal and vertical diffusivity coefficients in m^2/s , h is the mixed layer depth in m (defined as the depth
 275 where the density increase compared to density at 10 m depth corresponds to a temperature decrease of 0.2°C), T is the
 276 temperature in the mixed layer in K, \mathbf{U} is the horizontal current and w is the vertical velocity component both in m/s, Q_{net} is
 277 the net air-sea heat flux in W/m^2 . Brackets $\langle \cdot \rangle$ indicate the vertical averaging from the surface to the mixed layer depth.

a supprimé: (<

a supprimé: \gamma

a mis en forme : Anglais (E.U.)

a supprimé: $\frac{Residual}{RES}$ a supprimé: Q_{net}

282 The subscript h indicates the evaluation of the expression at the mixed layer depth. Each term of Eq (2-3) correspond to
 283 anomalies with respect to the daily climatology (as indicated by the prime) computed over 1993–2020.
 284 The net surface air/sea flux Q_{net} (counted as positive when entering the ocean and expressed in $W \cdot m^{-2}$) can be decomposed
 285 as:

$$Q_{net} = SW + LHF + SHF + LW - SW(-h) \quad (4)$$

286
 287 where SW is the net shortwave flux at the surface, $SW(-h)$ the shortwave flux leaving at the base of the mixed layer (light
 288 vertical penetrating function being parametrized following Paulson and Simpson, 1977 for type I water, Madec et al., 2024),
 289 LHF the net latent heat flux, SHF the net sensible heat flux, and LW the net longwave radiation flux. Concerning the
 290 residual, it encompasses several processes including: the effects of data assimilation, the entrainment at the base of the mixed
 291 layer (accounting for its space–time variability, vertical advection and lateral induction), and the horizontal/vertical turbulent
 292 mixing (see Eq. 3). However, at daily time scales this residual is generally dominated by vertical mixing (e.g. Dutheil et al.,
 293 2024). To quantify the contribution of each term during MHW events in terms of temperature evolution, the heat budget
 294 equation was integrated in time during the MHW from the event start (t_s):

$$\begin{aligned} & \langle T \rangle'(t) - \langle T \rangle'(t_s) \\ &= - \int_{t_s}^t \langle U(t) \rangle \cdot \nabla \langle T(t) \rangle' dt + \int_{t_s}^t \frac{Q_{net}}{\rho c_p h} (t)' dt + \int_{t_s}^t Residual(t) dt \end{aligned} \quad (5)$$

296 Following Elzahaby et al. (2022), at the peak time of each MHW, the contributions (integrated in time) of each term were
 297 assessed and compared to determine which term was dominant. Events were then categorized according to the dominant
 298 mechanism: **Q-MHW** when air-sea fluxes dominated, **HADV-MHW** when horizontal advection was dominant, **RES-**
 299 **MHW** when the residual term was dominant compared to Q and $HADV$ contribution separately as well as their sum, and
 300 **Mixed-MHW** when the relative difference between the Q and $HADV$ contributions was less than 10% of the total change of
 301 temperature from start to peak, and when their combined contribution was less than that of the residual term. For only a few
 302 events, none of the three terms on the right-hand side of Eq. (3) acted as positive drivers during MHW onset. These events
 303 were therefore excluded from the analysis.

304 To better understand the mechanisms controlling MHW onset and decay, the different terms of Eqs. (2) and (4), as
 305 well as wind (speed and direction), MLD, sea surface height (SSH) and surface oceanic currents anomalies were averaged
 306 over all MHWs occurring during the warm and cold seasons, separately. These averages were computed separately for each
 307 MHW type during the development phase, defined as the period from MHW onset to its peak intensity. During the decay
 308 phase, defined as the period from the peak to the end time, composites were constructed using all MHWs, including HADV,
 309 Q_s and RES-MHWs. The full terms of Eq. (2) for these composites can be found in Appendix A (Fig. A1, A2).

310

a supprimé: We chose here to consider a time-space varying MLD (and not a fixed seasonal or spatial average) as it has been shown that the identification of the dominant mechanisms at play during MHWs can change depending on the different MLD values when fixing a constant MLD . . .

a supprimé: towards

a supprimé:

a mis en forme : Anglais (E.U.)

a supprimé: $\langle T \rangle'(t) - \langle T \rangle'(t_s) = \int_{t_s}^t \langle U \rangle \cdot \nabla \langle T \rangle' dk + \int_{t_s}^t \frac{Q_{net}}{\rho c_p h} dk + \int_{t_s}^t Residual dk$

a mis en forme : Anglais (E.U.)

a supprimé: -level

a mis en forme : Anglais (E.U.)

a supprimé: of each type

a supprimé: for both

a mis en forme : Anglais (G.B.)

a supprimé: (

a supprimé: the

a supprimé: start time

a supprimé:) and

a mis en forme : Anglais (G.B.)

a mis en forme : Anglais (G.B.)

a mis en forme : Anglais (G.B.)

a mis en forme : Anglais (G.B.)

a mis en forme : Anglais (G.B.)

a supprimé: (

a supprimé:). For the decaying phase

a supprimé: (

a mis en forme : Anglais (G.B.)

a mis en forme : Anglais (G.B.)

a mis en forme : Anglais (G.B.)

a supprimé:) were used to build the composites

a mis en forme : Anglais (G.B.)

a mis en forme : Anglais (G.B.)

331 3- MHW characteristics across the central South Pacific and FP archipelagos

332 Figure 1, presents the median characteristics of past MHWs—including their number, intensity, and duration—detected in the
333 central South Pacific from 1981 to 2024 in OISST, shown separately for austral summer and austral winter. For each
334 archipelago, Fig. 2a–d displays the distribution of these characteristics, along with absolute and cumulative intensity, to
335 assess the level of MHW exposure across FP.

336 The total number of MHW days over the warm seasons of the period, expressed in mean number of MHW days per year is
337 heterogeneous across the region (Fig. 1a). It ranges from 7 to 13 days per year for central regions (Society-Tuamotu-
338 Gambier) and 13 to 18 days per year in the southwestern (Austral) and northeastern regions (near Marquesas) (Fig.1a).
339 During the cold season (Fig. 1d,e,f), most regions experience fewer MHW days compared to the warm season, with the
340 exception of the Austral and Gambier region, where the number of MHW days is comparable between the two seasons.

341 The most intense MHWs are observed north of 7°S and south of 25°S (Fig. 1b) leading to median maximum intensity values
342 of +1.7°C and +1.5°C in the Austral Islands during the warm and cold seasons, respectively (Fig. 2a). In the other
343 archipelagos, median intensity values range from +1.0 to +1.3°C. Across all archipelagos, MHWs are more intense during
344 the warm season than during the cold season, both in terms of median and extreme values (Fig. 2a,b). Due to the large
345 meridional extent of FP, climatological temperatures vary significantly from south to north (see Fig. S1). Absolute
346 temperatures reached are therefore quite different between the Austral and Marquesas. In absolute terms, the most intense
347 heat exposure is found over the Society, Tuamotu, and Marquesas archipelagos, with median values ranging from 27.6 to
348 28.4°C in the cold season and from 29.2 to 29.8°C in the warm season (Fig. 2b). The most intense heat exposure exceeds
349 30°C across most archipelagos during both seasons, except in the Gambier Islands (28.8°C and 29.8°C for the warm and
350 cold seasons, respectively) and in the Austral Islands during the cold season (28.8°C) (Fig. 2b).

351 The median duration is around 7-10 days for both seasons, with longer duration for the Marquesas region over the warm
352 season (Fig. 1c). Most MHW events are short-lived events, across all five archipelagos (Fig. 2d). Longer events are
353 particularly frequent in the Marquesas during the austral summer, where 25% of MHWs last longer than 19–20 days, 5% last
354 more than 50 days, and the longest MHWs exceed 250 days in both seasons. In the Austral Islands, the upper tail of the
355 duration distribution is also shifted upward compared to other archipelagos, with 5% of MHWs lasting more than 45 days in
356 both seasons. For the others, 75% of the distribution lies between 10 and 17 days.

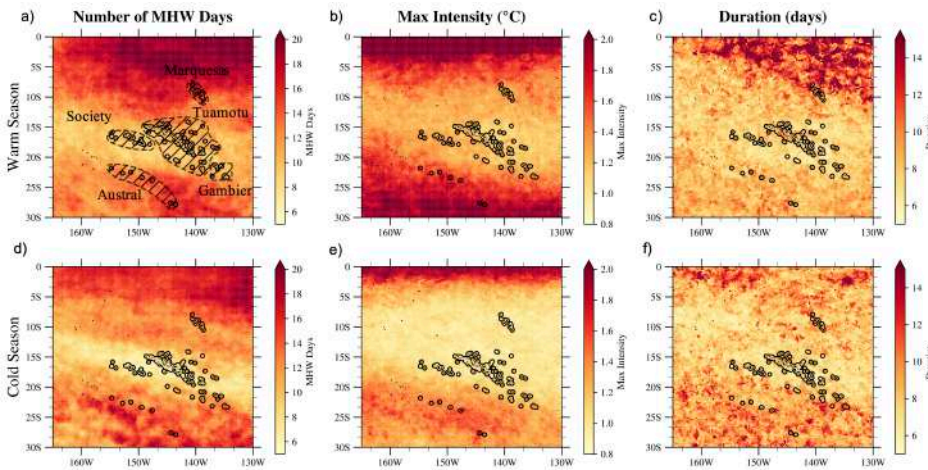
357 Cumulative intensity varies across FP in line with intensity and duration distributions (Fig. 2c). The Austral Islands (both
358 seasons) and the Marquesas (warm season) experience the highest cumulative intensities, with median values of 10 to
359 12 °C·days. In these regions, 25% of MHWs have cumulative intensities exceeding 20 °C·days, and 5% exceed 60 °C·days.
360 In the Society, Gambier, and Tuamotu Islands, median cumulative intensities are 7.8, 7.4, and 8.2 °C·days, respectively. In
361 these archipelagos, 25% of MHWs exceed 10 °C·days, and 5% exceed 30 °C·days—except in the Society Islands during the
362 warm season, where 5% of MHWs exceed 25 °C·days.

a mis en forme : Anglais (E.U.)

a supprimé: are

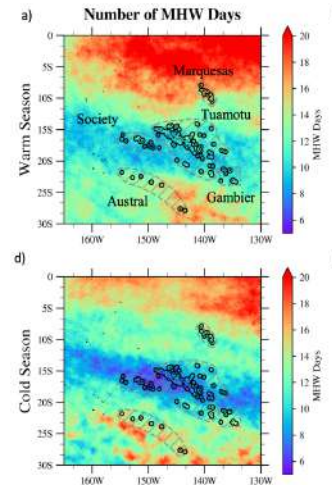
a supprimé: impacts

365 There is an overall positive trend of the number of MHW days over FP over the period for all archipelagos, as well
 366 as the area covered by MHWs over the FP region (Fig. 2e). Also, MHW occurrence varies greatly from year to year, and not
 367 similarly in each archipelago (Fig. 2e). In the Marquesas, several years may pass with few or no MHW events, followed by
 368 years with a very high number of MHW days.
 369 In the Austral Islands, MHWs are occurring more frequently each year, although substantial interannual variability remains,
 370 with some years—such as 2021 and 2022—characterized by a high number of MHW days.
 371 These differences led us to look at the link with ENSO (see Section 4).



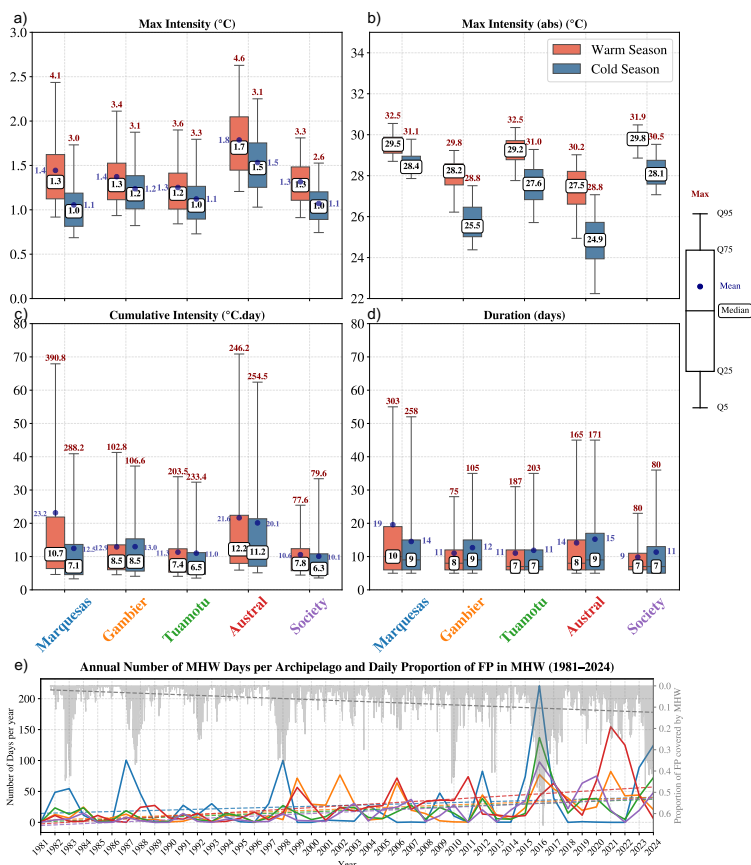
372
 373 **Figure 1.** Median characteristics of MHWs detected over the FP region for the period 1981–2024 in the OISST dataset. The total number
 374 of days in MHW expressed in mean number of days per year, maximum intensity (°C), and event duration (days) are displayed for the
 375 warm season (NDJFMA) in panels a, b, and c, respectively, and for the cold season (MJJASO) in panels d, e, and f, respectively. The
 376 names and locations of the archipelagos are shown in panel (a). The black dashed areas surrounding each archipelago in panel a represent
 377 the regions used to group MHW metrics by archipelago in Fig. 2.

- a supprimé: MHWs
- a supprimé: vary a lot
- a mis en forme : Anglais (E.U.)
- a supprimé: the same way
- a supprimé: happen
- a supprimé: regularly
- a mis en forme : Anglais (G.B.)
- a mis en forme : Anglais (G.B.)
- a mis en forme : Anglais (G.B.)
- a supprimé: bigger peaks
- a mis en forme : Anglais (G.B.)
- a mis en forme : Anglais (G.B.)



- a supprimé:
- a supprimé: gray

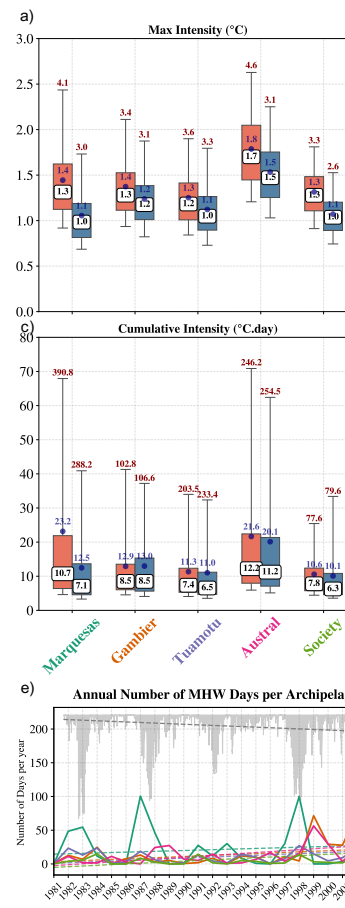
Marine Heatwave Metrics by Archipelago and Season



386

387 **Figure 2.** Panels (a–d) show MHW metric distributions for each archipelago area (see the black dashed area in Fig. 1a) for warm
 388 (NDJFMA, in red) and cold seasons (MJJASO, in blue). The box plots were generated from all MHW events detected at each grid point
 389 within the delimited regions around each archipelago shown on the Fig. 1a. Panels a–d show, respectively, the maximum intensity reached
 390 in each event, its absolute value, the cumulative intensity, and the duration. The whisker plot limits are indicated on the right side using a
 391 labeled box plot example. In panel b, the mean value is not shown because it is very close to the median, and displaying both would reduce
 392 the readability of the plot. The difference between the mean and median maximum intensity can be assessed in panel a. Panel (e) displays
 393 the annual evolution of the number of MHW days (thick lines) over each archipelago along with their linear trends (dashed lines). Line
 394 colors match the archipelago colors used on the x-axes of panels c and d. The estimated trend slopes expressed in MHW days per decade
 395 are 6.1 days.decade⁻¹ for the Marquesas (p = 0.26), 8.6 days.decade⁻¹ for the Gambier (p = 0.001), 8.5 days.decade⁻¹ for the Tuamotu (p =

Marine Heatwave Metric



a supprimé:

a supprimé: metrics'

a supprimé: map on

a supprimé: right

a mis en forme : Anglais (E.U.)

a mis en forme : Anglais (E.U.)

a mis en forme

404 0.002), 13.9 days.decade⁻¹ for the Austral Islands ($p \approx 10^{-6}$), and 10.2 days.decade⁻¹ for the Society Islands ($p \approx 10^{-5}$). The daily proportion
405 of FP covered by MHWs is shown in light gray, with its corresponding linear trend indicated by a gray dashed line. The slope of the gray
406 dashed line is 0.025 decade⁻¹ ($p < 10^{-7}$).

407

408 Additional metrics, such as onset and decline rate and maximum area, are provided in SI (Fig. S4). MHWs develop and
409 decay at a comparable pace across both seasons (MHWs develop slightly faster during the warm season than during the cold
410 season, not shown) and all archipelagos, with median growth rates ranging from 0.09 to 0.13 °C/day and decaying rates
411 ranging from 0.09 to 0.12 °C/day (Fig. S4a,b). MHWs occurring in the Marquesas tend to have larger spatial extents (median
412 of 1.7 million km² which is about 20% of the FP maritime Exclusive Economic Zone) compared to those in the Tuamotu,
413 Society, Austral, and Gambier Islands, where median values range from 400,000 to 600,000 km². Moreover, large MHWs
414 (more than 10⁶ km²) are more frequently detected over the Tuamotu and Society Islands than in the Austral and Gambier
415 Islands.

416 Equivalent analyses [to those](#) of Fig. 1 and 2 using the detrended MHW dataset are also available in Fig. S5, S6. In brief,
417 detrending the data does not alter the differences observed between archipelagos but slightly reduces MHW intensities across
418 all regions, except in the Marquesas where the SST trend is weak and negative (Fig. S2). Detrending also reduces MHW
419 duration across all archipelagos. Consequently, cumulative intensity is slightly reduced everywhere except in the Marquesas,
420 where it is a bit increased. Additionally, detrending leads to a slight increase in the onset rate of MHWs.

421 The same analysis for MHWs detected in GLORYS over 1993-2024 is shown in SI (Fig. S7). For [the FP region](#), median
422 values and inter-archipelagos differences are consistent between OISST and GLORYS. However some differences can be
423 seen, detected MHWs are generally longer and weaker in GLORYS than in OISST [in agreement with](#) Pilo et al., (2019) and
424 Chevillard et al., (2025). Despite these differences, the coherence between the products gives us confidence in the ability of
425 GLORYS to simulate the past MHWs realistically, [and thus to analyze processes underlying MHWs in GLORYS \(cf section](#)
426 [5\)](#).

427

428 4- ENSO as a driver of MHWs

429 We now analyse the link between ENSO and MHWs properties, and examine the modulation of MHWs by ENSO. In section
430 4.1, we first simply separated days into [El Niño \(EN\)](#), [La Niña \(LN\)](#) or [Neutral \(N\)](#) conditions ([without differentiating](#)
431 seasons, cf. Methods for identification of EN and LN periods). Section 4.2 [discusses](#) ENSO spatial diversity/flavors using
432 [the](#) Pagli et al. (2025a,b)'s classification. MHWs analyzed here are those detected in the detrended SST of OISST (cf.
433 section 2.2).

a supprimé: per

a mis en forme : Anglais (G.B.)

a supprimé: IM

a supprimé: of that

a supprimé: that

a supprimé: .

a supprimé: .

a mis en forme : Anglais (E.U.)

a supprimé: .

a supprimé: all

a mis en forme : Anglais (E.U.)

a supprimé: taken into account

a supprimé: The next section (

a supprimé:) will discuss

a mis en forme : Anglais (E.U.)

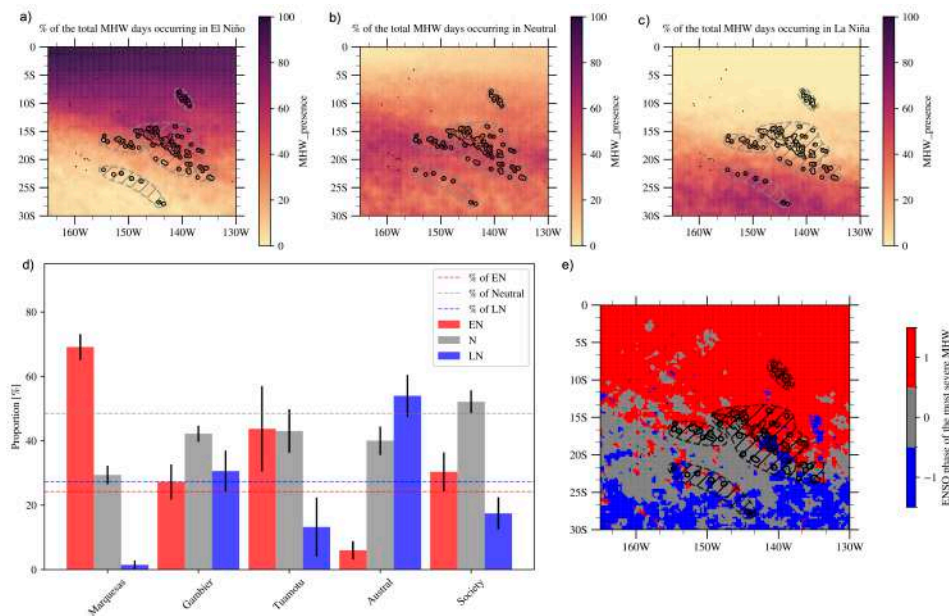
a mis en forme : Anglais (E.U.)

a mis en forme : Anglais (E.U.)

445 **4.1- Modulation of MHW occurrence and intensity**

446 Figure 3a–c shows the proportion of MHW days occurring during EN, N, and LN conditions at each grid point. Using the
447 proportion of MHW events starting in EN/LN/N instead of days does not change the conclusions (not shown). A clear spatial
448 modulation of MHWs by ENSO emerges. During EN, MHWs are more frequent in the northeast region—from the Society
449 and northern Tuamotu to the Marquesas—where up to 70% of MHW days occur during EN (Fig. 3d). In contrast, MHWs are
450 less common in the Austral islands during EN, accounting for only 5% of MHW days (Fig. 3d). During LN, the spatial
451 distribution of MHW shifts southwestward, with ~60% of MHW days in the Austral islands occurring during this phase (Fig.
452 3d). In the central region, where MHWs mostly occur during N periods (Fig. 3b), EN still enhances MHW occurrence over
453 the Society and Tuamotu archipelagos (Fig. 3d). For the Gambier Islands, EN and LN show no significant effects (Fig. 3d).
454 Figure 3e shows the ENSO phase associated with the start time of the most severe MHW (in terms of S, cf. section 2.2) at
455 each grid point, which closely aligns with the spatial modulation patterns described above. The most intense MHWs in the
456 northeastern region (north and east Tuamotu and Marquesas) tend to occur during EN, while those in the southwestern
457 region (Austral and south Tuamotu) are mostly associated with LN. In the central region (Society, west Tuamotu, Gambier),
458 the signal is more variable, but the most severe events are triggered during neutral phases.

459

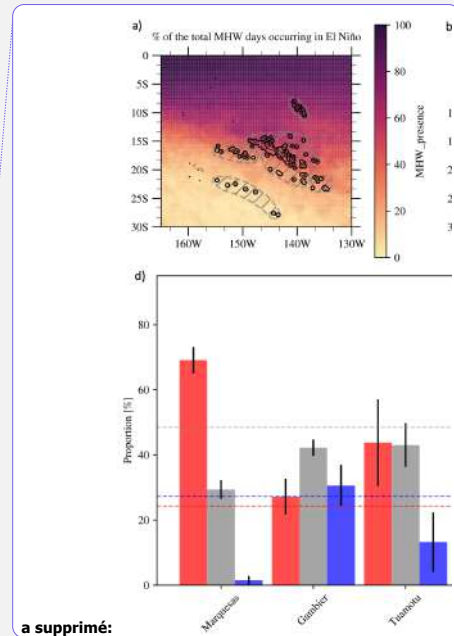


460

461 **Figure 3.** Proportion of MHWs occurring during different ENSO phases: El Niño (panel a), Neutral (panel b), and La Niña (panel c).
 462 Panel d shows the average percentage of MHWs associated with each ENSO phase for the five archipelagos of FP. The horizontal dashed
 463 bars indicate the proportion of El Niño (red), La Niña (blue), and Neutral (gray) days over the study period (1981–2024). Comparing the
 464 bars with the same-colored dashed lines—showing the fraction of El Niño/La Niña/Neutral days in that period—reveals how strongly
 465 ENSO modulates MHW occurrence. Black error bars indicate the spatial standard deviation of the statistics calculated across grid points
 466 associated with each archipelago area (black dashed outlines in panel e). Panel e shows the ENSO phase associated to the start time of the
 467 most severe MHW at each grid point (defined following the categories of Hobday et al., 2018, cf. Methods). SST was detrended prior to
 468 MHW detection for this analysis (similar results were obtained without removing the trend, not shown). The same figure for austral and
 469 boreal summer MHWs separately is shown in SI, Fig. S8-S9. Also, similar modulation is obtained in GLORYS over the same period (not
 470 shown).

471

472 Similar conclusions were obtained with MHWs detected without having removed the trend in OISST as well as with MHWs
 473 detected in GLORYS over the same period (not shown). As shown in SI (Fig. S8 and S9), the MHW spatial patterns
 474 modulated by ENSO revealed in Fig. 3 are exacerbated during austral summer (NDJFMA) during the peak of ENSO events
 475 but weakened during austral winter (MJJASO). We therefore focus on the austral summer season for a more in-depth
 476 analysis that includes ENSO diversity.



a supprimé:

a supprimé: has been

a mis en forme : Anglais (E.U.)

a supprimé: by detecting MHWs

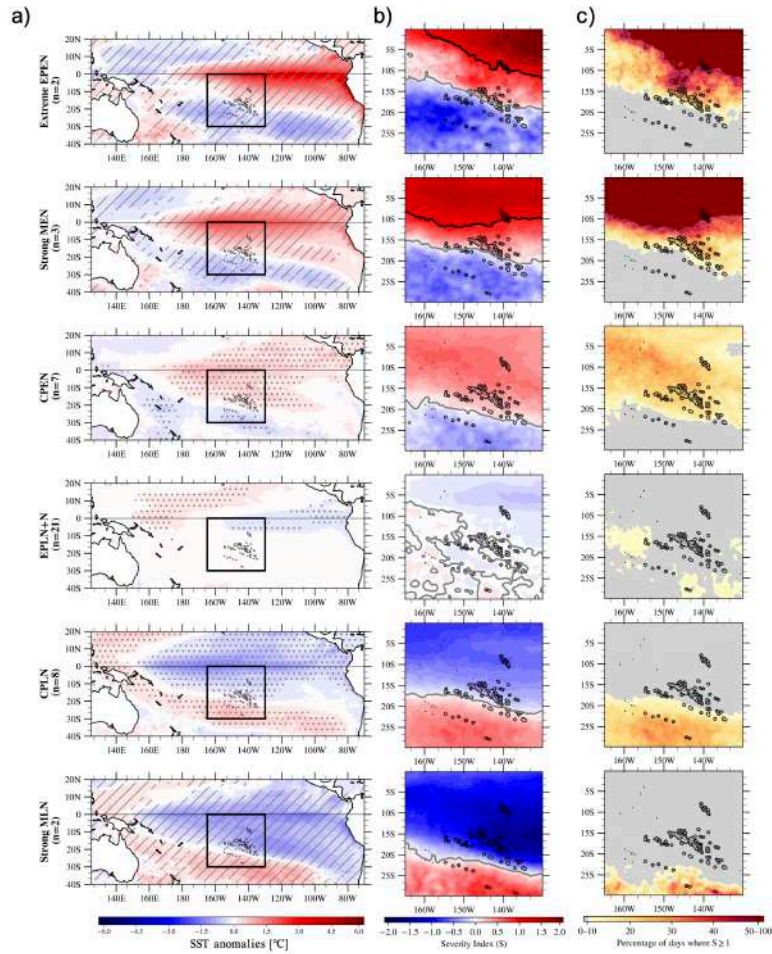
a supprimé:

a supprimé: have been

482 4.2- Modulation of MHWs by the diverse flavors of ENSO

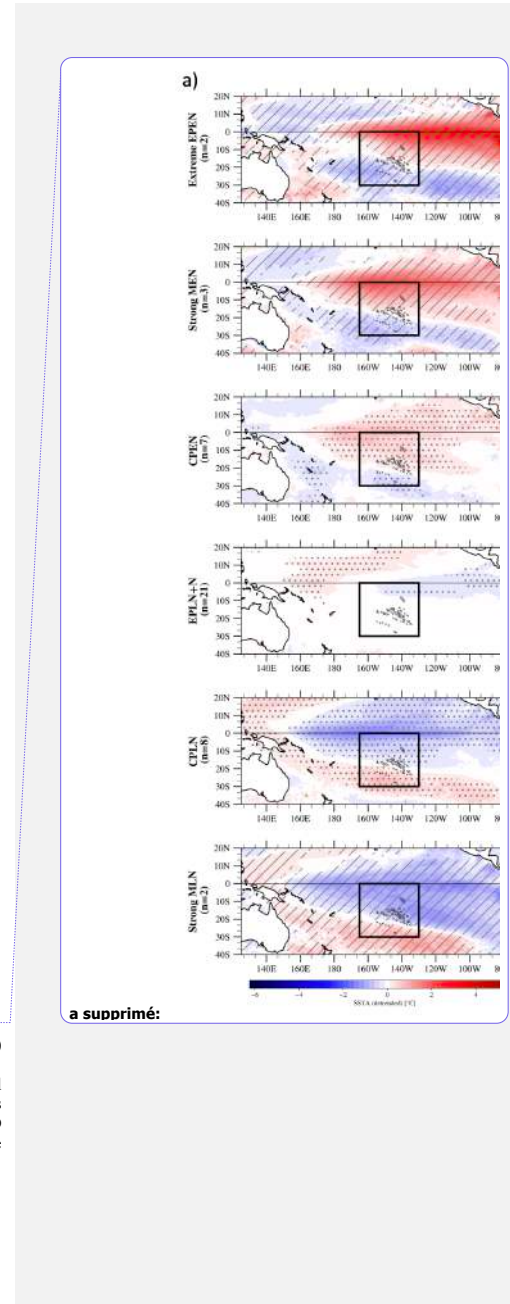
483 There is an important diversity of ENSO impacts during austral summer over FP especially in terms of SST intensities and
484 spatial patterns (Pagli et al., 2025a and Fig. 4a). Figure 4 recalls the six ENSO clusters defined by Pagli et al. (2025a,b) at
485 the FP scale (cf. section 2.2 and Table S1). NDJFMA composites (average across years of each cluster) of SST anomalies at
486 the Pacific scale (in °C) and local scale (expressed in terms of S index) are shown in panels a and b, respectively. The
487 composite of the percentage of days where $S \geq 1$ is shown in panel c. Figure 5 highlights how the different ENSO flavors
488 impact cumulative heat stress over the warm season at the FP scale, as depicted by DHW that takes into account the time
489 integration of the heat stress and is recognized as an indicator of coral bleaching. The maximum of DHW reached for each
490 austral summer averaged over years from each ENSO clusters is displayed in Fig. 5a and the same quantity averaged over
491 each archipelago and for each year of the period is displayed in Fig. 5b-f. In SI (Fig. S10), MHW intensity, duration, and the
492 number of MHW days composited for each ENSO cluster are displayed.

a mis en forme : Anglais (E.U.)



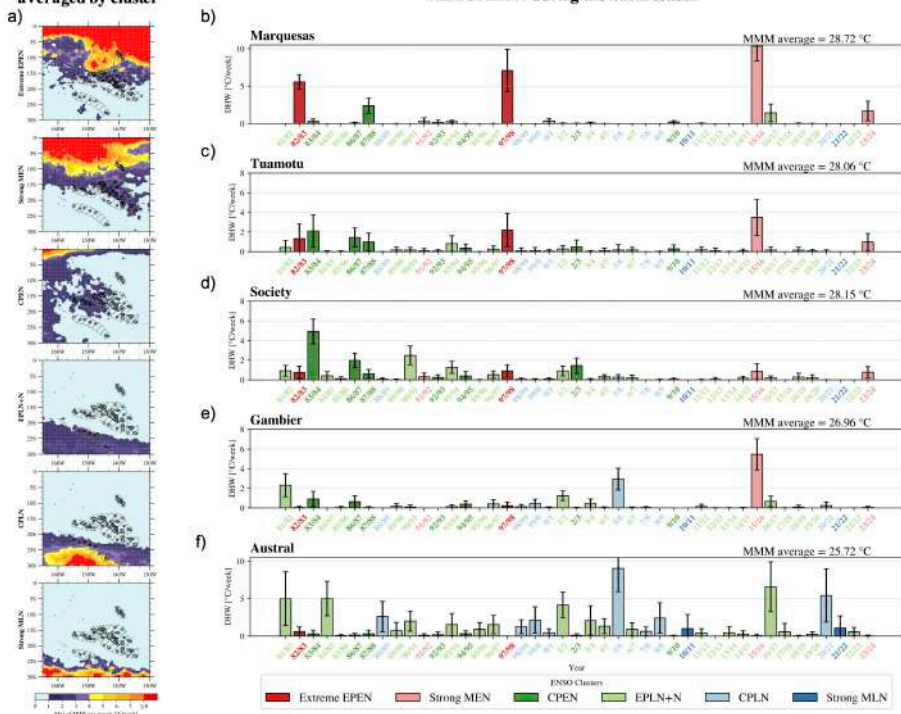
493

494 **Figure 4.** Composites of SST anomalies (linearly detrended) averaged over NDJFMA for the ENSO classification of Pagli et al., (2025a,b)
 495 at the Pacific scale (a). Cluster composites of S for NDJFMA are shown in the panel b, with isolines corresponding to $S = 0$ and $S = 1$
 496 displayed in gray and black, respectively. The cluster composites of the percentage of days where $S \geq 1$ over NDJFMA is shown on panel
 497 c. Gray (dark red) area corresponds to regions where 0 to 10% (50-100%) of the NDJFMA days satisfy this criteria. In panel a, dots
 498 indicate anomalies significant at the 90% confidence level based on a two-tailed Student t-test. The number of years (n) in each ENSO
 499 cluster is indicated on the y-axis of panel a. For clusters spanning two or three years, gray hatching marks regions where anomalies share
 500 the same sign across all years in the cluster.



a supprimé:

Max of DHW during the warm season averaged by cluster



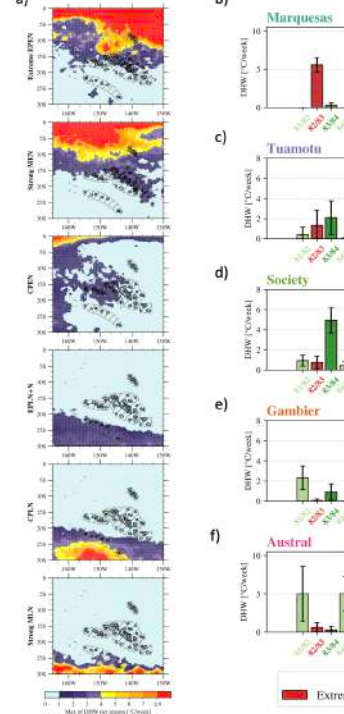
503

504 **Figure 5.** ENSO cluster composites of the maximum of DHW over the warm season (a) and yearly maximum of DHW averaged over each
 505 archipelago region (b-f). For each archipelago, the spatial average of the Maximum Monthly Mean (MMM) used to compute the DHW is
 506 indicated on the top right of panels b-f. Year labels on x-axis and bars are colored by ENSO cluster. The black error bars show ± 1 standard
 507 deviation across all pixels within each archipelago area. These results were computed using detrended SST data; for DHW values based on
 508 non-detrended SST data, see Fig. S11.

509

510 Figure 4 refines the ENSO modulation of MHWs during the warm season, as introduced in section 4.1 (Fig. 3). On average
 511 over the austral summer, during strong EN events, classified in strong Mixed EN (MEN) and extreme Eastern Pacific EN
 512 (EPEN) clusters, the Marquesas region and equatorward areas remain in a MHW state throughout the entire summer (90–
 513 100% of MHW days, and $S \geq 1$ on average over the 6 months; see Fig. 4b,c). These MHWs are very long and intense (Fig.

Max of DHW by Warm Season averaged by cluster



a supprimé:

515 S10b,c), resulting in exceptionally strong cumulative heat stress over this region (Fig. 5a). Further south, MHWs are favored
516 ($0 < S < 1$) in a band extending from the Marquesas to northern Tuamotu and Society Islands only (Fig. 4b,c). Over this
517 MHW-favored area, the proportion of days with $S \geq 1$ during the warm season increases gradually from south (10%) to north
518 (50%). In contrast no MHWs are detected in the far southern regions during strong MEN and extreme EPEN events. During
519 Central Pacific EN (CPEN), all archipelagos—except the Austral Islands—experience SSTs warmer than usual (Fig. 4a),
520 though still below the MHW threshold on average over the austral summer (Fig. 4b). These warmer SST favor MHW
521 development and result in an average of ~30% MHW days during the warm season (Fig. 4c), with a slight increase of
522 cumulative heat stress on average for central regions (Fig. 5a). Conversely, in the southwest, S values are on average
523 negative (Fig. 4), indicating unfavorable conditions for MHWs. During neutral years to weak LN (EPLN+N), S anomalies
524 across FP are weak and close to zero, only a few MHWs occur during some of these years over this region. During Central
525 Pacific LN (CPLN-englobing most of the LN events), MHWs are favored in the southern Society Islands, extreme south
526 Tuamotu, and the Gambier Islands, with around 20–30% of MHW days over the warm season. MHWs are generally
527 unfavored elsewhere. This leads to an increase of cumulative heat stress in the Austral Islands (Fig. 5a). Finally, during
528 strong Mixed LN (MLN) events, MHWs are favored exclusively in the extreme south of the Austral Islands (i.e., Rapa Iti),
529 where they are associated with strong cumulative heat stress, while unfavorable conditions prevail across the rest of FP (Fig.
530 5a).

531 Periods of increased cumulative heat stress coincide spatially with positive SST anomalies associated with the ENSO
532 clusters. However, the magnitude of DHW can vary from year to year even for similar mean SST anomalies over the season
533 and across archipelagos. This is because it reflects the time-integrated effect of SST anomalies and therefore the risk for
534 coral bleaching is not systematically reached where ENSO-related SST anomalies are positive (Fig. 5b-f). In the Marquesas,
535 very strong cumulative heat stress occurred during the 1982/83, 1997/98, 2015/16, and 2023/24 El Niños (extreme EPEN and
536 strong MEN) while 1991/92 (a strong MEN) was comparatively associated with weaker cumulative intensity (Fig. 5b). We
537 can note also that 1987/88 (CPEN) produced a strong heat stress over the Marquesas. In the Tuamotu, the same years in
538 addition to 1983/84, 1986/87 (CPEN) are linked to the highest cumulative heat stress (Fig. 5c), but with lower cumulative
539 heat stress than in the Marquesas. Interestingly, the 1991/92 strong MEN event, despite being extreme for FP in terms of
540 SPCZ displacement and tropical cyclone activity (Vincent et al., 2011; Pagli et al., 2025a,b), was not as intense in terms of
541 MHWs over the Marquesas and Tuamotu. In the Society archipelago, 1983/84, 2009/10, 2002/03 (CPEN) and neutral years
542 1990/91, 2016/17 (EPLN+N) correspond to the strongest DHW values (Fig. 5d). While strong MEN and extreme EPEN
543 years also produce considerable cumulative intensities in this region, they are not the highest, highlighting that the strongest
544 EN events (as defined on a global scale) do not always correspond to the most severe impacts over FP. In the Gambier
545 Islands, both EN and LN events can produce significant cumulative heat stress (2005/06 CPLN and 2015/16 strong MEN)
546 during the warm season (Fig. 5e), with no consistent influence of specific ENSO clusters on the cumulative heat stress. This
547 aligns with the unclear ENSO modulation highlighted for the Gambier Islands in Fig. 3. In the Austral Islands, the strongest
548 cumulative heat stress are observed in 1988/89, 2005/06 and 2020/21 LN years, particularly CPLN events.

a supprimé: year

550 These conclusions were drawn from analyses based on detrended SST data, aiming to isolate the ENSO imprint on
 551 cumulative heat stress over FP. However, when using the non-detrended SST data —which reflects the total heat stress
 552 exposure experienced at the surface —the maximum DHW values over the warm season for years occurring after 2000 are
 553 amplified over the Tuamotu, Society, and Gambier archipelagos (Fig. S11) especially in 2015/16 (strong MEN) that has been
 554 associated with massive wide coral bleaching over FP (Hédouin et al., 2020) and more recently in 2023/24 (strong MEN).

a supprimé: in

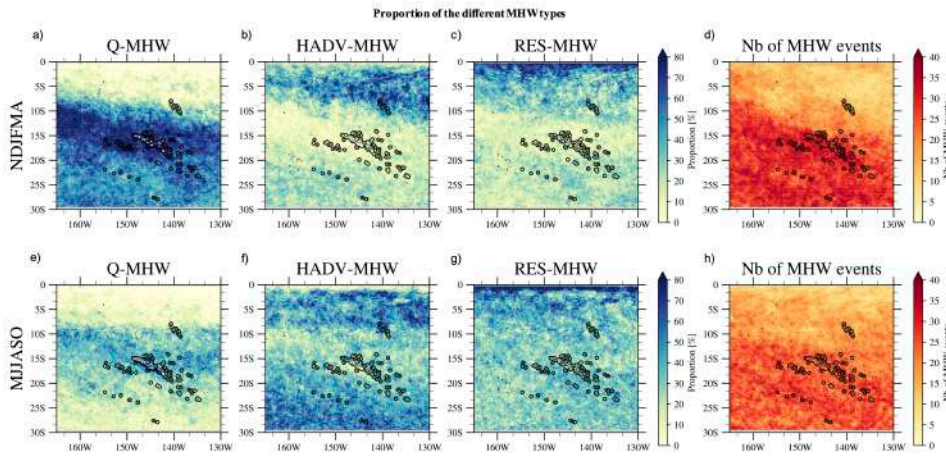
555 5- Physical mechanisms generating and dissipating MHWs over 1993-2020

556 5.1- MHW development

557 In this section we investigate the physical mechanisms of the MHWs in the GLORYS oceanic reanalysis (over the 1993-
 558 2020 period, see Methods in section 2.2). We examined the dominant local mechanisms of MHWs development across the
 559 territory for austral summer and winter separately (Fig. 6) — focusing on air-sea surface heat fluxes, horizontal advection,
 560 and residual terms (see Eq. 2). The residual term consisted mainly of the vertical/horizontal mixing and entrainment at the
 561 bottom of the mixed layer plus implicit heat sources/losses due to the assimilation in GLORYS (see Eq. 3). Also, because the
 562 vertical mixing may be poorly represented in GLORYS (due to the lack of explicit tidal forcing) and because the magnitude
 563 of the data-assimilation increments is unknown here, interpreting in detail this residual is beyond the scope of this study.

a supprimé: consists firstly

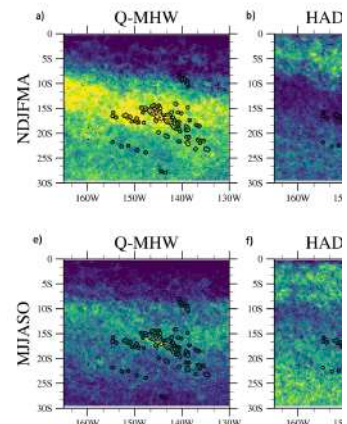
564



565

566 **Figure 6.** Proportion of the different MHW types for all events detected in austral summer and austral winter separately (d,h) in GLORYS,
 567 during the 1993-2020 period. Panels a and e show the proportion of Q-MHWs in austral summer and winter, respectively; panels b and f
 568 show HADV-MHWs; panels c and g show RES-MHWs. Mixed events are not shown, as they represent only a small number of cases.

a supprimé:



572 MHWs are driven by different mechanisms depending on the region and the season (Fig. 6), and a strong differentiation
573 appears at about 10°S. During austral summer, MHWs are primarily driven by air/sea fluxes in most archipelagos south of
574 10°S, especially in the central regions (Society and central Tuamotu), accounting for 70–80% of total events (Fig. 6a).
575 HADV-MHWs and RES-MHWs represent 0 to 30% of the total events except for MHWs occurring in the equatorward
576 region, north of 5°S/10°S (Fig. 6b,c). Here, HADV-MHWs dominate and account for 60–70% of the events south of 2°S.
577 The residual becomes dominant in a thin equatorial band due to the particular dynamics of the region with notably the
578 equatorial upwelling (e.g. Deppenmeier et al., 2021). During austral winter, the proportion between MHWs types is more
579 balanced in central regions with a slight dominance of Q-MHWs compared to HADV-MHWs and RES-MHWs (Fig. 6e,f,g).
580 HADV-MHWs proportion increases across the southern subtropical region (south of 20°S) compared to summer accounting
581 for more than 60% of total events. RES-MHWs proportion slightly increases across FP in winter compared to summer too.
582 Following our classification criteria (cf. section 2.2), mixed-MHW were almost never defined over both seasons (not
583 shown).

584

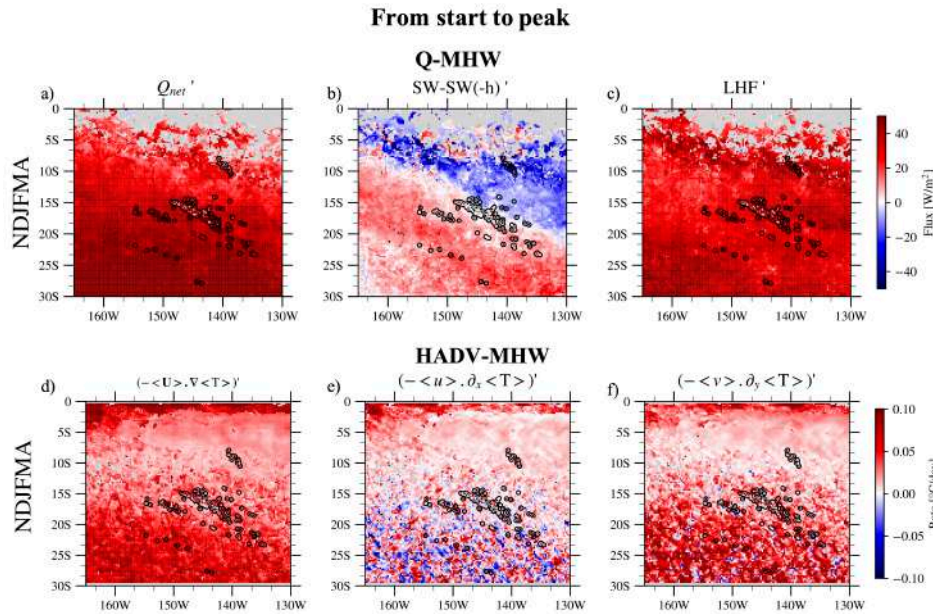
585 We now look at the mechanisms of MHW development for Q-MHWs and HADV-MHWs separately. For each MHW type,
586 the terms in Eq. (2) were averaged from start to peak at each grid point and then composited over all events for austral
587 summer and winter separately (Fig. A1). Only the results for the austral summer MHWs are presented in this section and
588 those for austral winter MHWs are available in Appendix A. The standard deviation associated to the mean composites
589 presented in Fig. A1 and A2 are presented respectively in Fig. S12 and S18. Because Q-MHWs are, by construction,
590 dominated by the air–sea heat budget term contribution, we focus on Q_{net} and its leading components, shown in Fig. 7a–c.
591 Conversely, since HADV-MHWs are driven by horizontal advection contribution, we focus in Fig. 7d–f on the horizontal
592 heat advection term and its zonal and meridional components. MLD (full field and anomalies), wind, SSH, and surface-
593 current anomalies are shown in Fig. 8. These results for austral winter are available in SI.

a supprimé: flux-

a mis en forme : Anglais (E.U.)

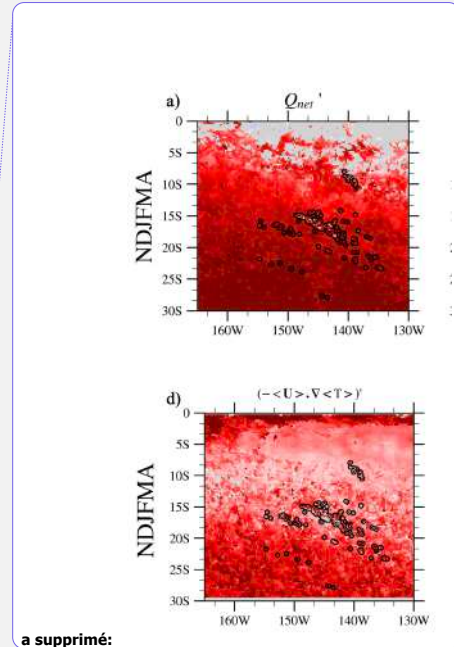
a mis en forme : Anglais (E.U.)

a supprimé: (the vertical terms and heat increments due to data assimilation) becomes dominant in a thin equatorial band due to the



597

598 **Figure 7.** Composites of the net air–sea heat flux (and its dominant components : SW-SW(-h) and LHF) for Q-MHWs and of the
 599 horizontal-advection term (and its decomposition into zonal and meridional components) for HADV-MHWs, for events peaking in the
 600 warm season (NDJFMA), averaged over the onset-to-peak period (cf. section 2.2). Panels a–c show Q-MHW composites of (a) net air–sea
 601 heat flux Q_{net} (b) the net shortwave flux stored in the mixed-layer ($SW - SW(-h)$), and (c) LHF anomalies. Panels d–f show HADV-
 602 MHW composites of (d) horizontal advection and its (e) zonal and (f) meridional components. In each panel, the composite corresponds to
 603 the averaged across all MHWs of the corresponding type (Q-MHW or HADV-MHW) detected at each grid point.



628 Results are broadly similar across seasons (Fig. A1e-h Fig. S14a-c, and Fig. S13d-f). During austral winter—when the
629 seasonal mixed layer is thicker—the required LHF anomalies, and thus the wind-speed anomalies needed for Q-MHWs to
630 develop, are larger than in austral summer (Fig. S17a,b,c). This also explains why Q-MHWs are more frequent in austral
631 summer than in austral winter (Fig. 6a,b). Also, in winter, SW variations during MHW development are highly event-
632 dependent with no clear pattern on the composite shown in Fig. S14b. They can either reinforce or damp the warming
633 associated to reduced evaporation (Fig. S14a,b,c).

634

635 HADV-MHWs

636 North of 10° S (but south of 3°S, out of the equatorial wave guide)—where most HADV-MHWs occur during EN (cf. Fig. 3
637 and 4)—both zonal and meridional heat advection contribute (Fig. 7d,e,f). The warming during the onset is associated to
638 eastward current anomalies that transport the climatologically warmer waters from the west (Fig. 8h, $u' \cdot \partial_x T$ in the $\mathbf{U}' \cdot \nabla T$
639 term, Fig. S16g, h). In addition, the EN-enhanced SST gradient is advected by the mean circulation to higher latitudes,
640 fueling HADV-MHWs' onset south of 10° S and up to 20°S ($\mathbf{U} \cdot \nabla T'$ term, Fig. S16d,e,f).

641 Moving southward, the signal becomes noisier, but meridional advection shows the most systematic warming during the
642 development stage (Fig. 7f). This arises from persistent southeastward anomalous currents that can be forced directly by
643 wind anomalies (Fig. 8g, h) and/or from geostrophic adjustment and/or from anomalous circulation linked to westward-
644 propagating anticyclonic eddies (positive SSH, Fig. 8h; the composite method, done for MHWs at each grid point separately,

645 smooths out eddy patterns, with only their SSH contribution during the MHW's onset at the grid point being visible), which
646 likely also contribute to the noise seen in Fig. 8h.

647 Air-sea flux contributions during HADV-MHWs are less systematic as shown by the noise present in the composite in Fig.
648 A1j, sometimes reinforcing the advective warming and sometimes damping it from one event to another. Nevertheless, in the
649 Marquesas—where most events occur under EN—the net air/sea heat flux term tends, on average, to damp the MHW
650 development (Fig. A1j). Southwest of the Marquesas, over other archipelagos, the air/sea flux term generally provides a
651 slight warming, though with strong event-to-event variability (Fig. A1j). Conclusions about the onset mechanisms of
652 HADV-MHWs are very similar in austral winter (Fig. A1m-p).

653 The residual term contribution to MHW onset composited for Q-MHWs and HADV-MHWs presents a strong inter-event
654 variability and is hard to interpretate here (Fig. A1d, h, l, p). On average, for MHWs occurring north of 10°S, the residual
655 term contributes to the warming of the mixed layer during the MHW onset for both Q- and HADV-MHWs and over both
656 seasons. This may be linked to reduced vertical mixing caused by the weaker winds and shallower MLD observed during the
657 MHW development (Fig. 8b, c, f, g and Fig. S17b, c, f, g).

658 RES-MHWs constitute a substantial fraction of events over FP (Fig. 6c,g). Fig. A1q-x shows the composites of the different
659 terms of Eq. (2) during their onset. By construction, their development is driven by the residual term which may be
660 dominated by vertical processes (mixing and entrainment), while contributions from air-sea fluxes and horizontal heat
661 advection are highly variable from event to event and show no systematic pattern.

a mis en forme : Anglais (E.U.)

a mis en forme : Anglais (E.U.)

a mis en forme : Anglais (E.U.)

a supprimé : smooth

a supprimé : eddies pattern

a supprimé : to

a supprimé : MHW

a mis en forme : Anglais (G.B.)

a supprimé : Up to now we did not comment on the role of the residual term during the onset and decay of Q- and HADV- MHWs.

a supprimé : present

a supprimé : hardly interpretable

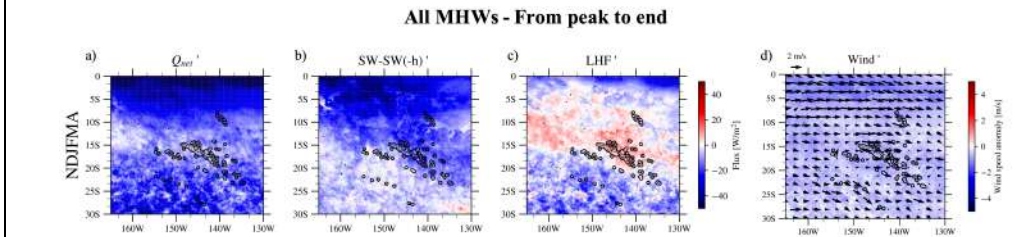
670

671 5.2- MHW decay

672 We now investigate the decay stage (peak to end) of MHWs over FP. As the classification into different MHWs types has
673 been solely designed for the developing phase (classification criteria applied regarding the terms contribution integrated
674 from onset to peak time, cf. section 2.2), we used all MHWs together to study the decaying stage of MHWs (after verifying
675 that decaying mechanisms do not significantly differ between MHWs types).

676 In austral summer, the transition from onset to decay (Fig. 9a,d) is dominated by cooling from the air-sea heat-flux budget
677 term of Eq. (2) (Fig. A2). It is mainly due to negative Q_{net} anomalies that are mainly explained by the anomalies of the net
678 SW in the mixed-layer in the north and of surface LHF in the south (Fig. 9a, b, c). Over the northeastern half of FP, it is the
679 negative incoming SW anomalies that explain the most the cooling of mixed-layer temperature while LHF' continues on
680 average to warm but with a strong inter-events variability. In the southwestern half, it is more systematically the cooling due
681 to negative LHF anomalies i.e. increased evaporation that causes the decaying of MHWs. This can be due to increases in
682 wind speed and/or SST or to a decrease in air moisture above the ocean surface (a drier air mass increasing evaporation).
683 When looking at the composite of the wind speed anomalies for the MHW decay (Fig. 9d), these are still negative, but less
684 than during onset, meaning that MHW warm SST and/or decrease in the surface atmosphere moisture may play a role.

685 In austral winter, the role of SW anomalies weakens and on average MHW decay is caused mainly by negative LHF
686 anomalies that are more systematically associated to positive or neutral wind speed anomalies (Fig. S19), with possibly also
687 a role of warm SST.



688

689 **Figure 9.** Composites of the net air-sea heat flux (and its dominant components) as well as surface wind anomalies averaged over the
690 decay period i.e. from peak to end (cf. Methods) for all MHWs peaking in austral summer. Panels a-c show MHW composites of (a) net
691 air-sea heat flux Q_{net} (b) the net shortwave flux in the mixed-layer ($SW - SW(-h)$), and (c) LHF anomalies. In each panel, the composite
692 is averaged across all MHWs (without distinguishing by type as done during the onset period) detected at each grid point.

693

694 During MHW decay, the residual term is more spatially coherent and exhibits less noise (Fig. A2d,h) than during the onset
695 for Q- and HADV-MHW types (right column of Fig. A1). In austral summer, it produces anomalous warming of the mixed

a mis en forme : Anglais (E.U.)

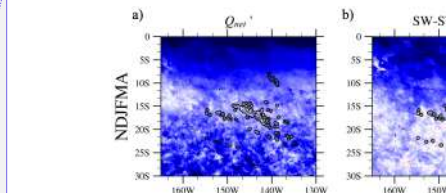
a mis en forme : Anglais (E.U.)

a mis en forme : Anglais (E.U.)

a mis en forme : Anglais (E.U.)

a supprimé: surface

a supprimé: back to normal



a supprimé:

699 layer; in austral winter, it warms north of ~10°S and cools south of ~15°S. The nature of the residual is complex and can
700 result from different processes. The ability of their parametrization in GLORYS, and the increments of data assimilation vary
701 in space and time. Our approach (heat budget not completely closed in a reanalysis) does not allow us to interpret more in
702 depth this residual term. Modeling approaches capable of accurately resolving this term could enhance our understanding of
703 the underlying processes.

704

705 5.3- The role of ENSO

706 The role of ENSO and its diversity in modulating the spatial distribution of MHWs has been highlighted in section
707 3.2 (Fig. 3, 4, 5). The preceding details on the mechanisms involved during the onset and decay phases of MHWs across FP
708 further help to understand ENSO's influence. EN generates positive SST anomalies over the northeastern half of FP and
709 negative anomalies over the southwestern half, with the opposite pattern observed during LN (Fig. 4). These SST anomalies,
710 depending on their signs, reduce or increase the gap to the MHW threshold depending on the region, thereby creating a
711 favorable or unfavorable background state for MHW development. Figure 10 displays surface wind, mixed layer, SSH and
712 surface currents averaged for EN and LN separately. EN periods are characterized by a significant shoaling of the mixed
713 layer, and reduced wind speeds across most archipelagos, therefore creating a favorable environment for MHWs
714 development (by reducing evaporation, rendering the mixed-layer more sensitive to warming from air/sea fluxes and
715 potentially also reducing the efficiency of vertical processes – upwelling, mixing, entrainment - in cooling the mixed layer)
716 over most regions except around Austral Islands (Fig. 10a,b). In addition to that, eastward current anomalies to the north
717 bring warmer waters from the west and induce deeper thermocline over the northeastern part. Conversely, LN periods are
718 associated with a deeper mixed layer over most regions, limiting the MHWs' development. Furthermore, LN events are
719 associated with a deeper (shallower) thermocline to the southwest (northeast) and a shallower mixed layer and weaker winds
720 over the Austral Islands and their southwestern margins due to the anomalous northwesterly winds (Fig. 10e). This clearly
721 aligns with the spatial modulation of MHWs by ENSO revealed in Fig. 3. ENSO thus acts as a large-scale forcing over FP,
722 promoting the development of MHWs in some regions while inhibiting them in others. Although a full characterization of
723 how different ENSO flavors modulate MHW mechanisms is beyond the scope of this study, Fig. 4–5 suggest that both the
724 spatial pattern and the amplitude of wind, mixed-layer and currents interannual anomalies likely depend on the ENSO flavor,
725 consistent with flavor-dependent wind and precipitation anomalies (Pagli et al., 2025a). This can explain the differences
726 observed in MHW properties and occurrences during the different EN and LN flavors (Fig. 4,5, S10).

727

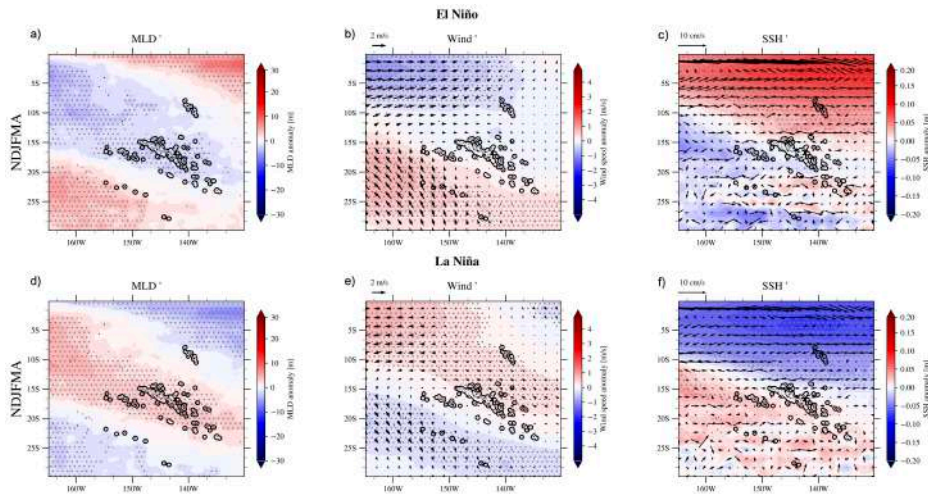
a supprimé: to represent them

a supprimé: may

a supprimé: reduce

a supprimé: terms

a mis en forme : Anglais (E.U.)

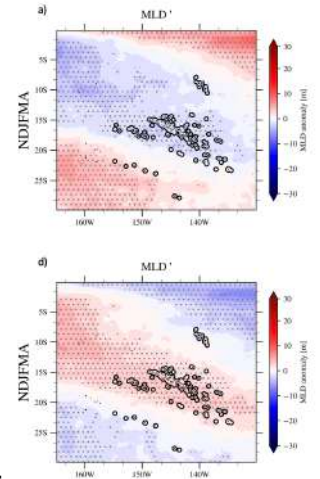


732

733 **Figure 10.** Austral summer El Niño and La Niña composites of the MLD (a,d), 10m-wind speed and direction (b,e), SSH and oceanic
 734 horizontal currents averaged from the surface to 30m (c,f) anomalies. Gray dots mark anomalies significant at the 95% confidence level
 735 (two-tailed Student t-test). The effective number of degrees of freedom have been computed as $n \frac{(1-\rho_1)^2}{(1+\rho_1)}$ following Bretherton et al.,
 736 (1999) where ρ_1 is the lag-1 autocorrelation of the each field and n is the total number of timestep (number of days here).

737 **6- Discussion**

738 Our results regarding the classification of MHWs into different **types** (Q, HADV, RES) over the South Central Pacific (Fig.
 739 6) align with previous global modeling studies investigating dominant MHW mechanisms with mesoscale-resolving models
 740 (Marin et al., 2022, Bian et al., 2023,2024) when looking at the spatial repartition of Q-MHWs and HADV-MHWs
 741 dominated-regions. It is interesting to note that the conclusions obtained here about the mechanisms of all MHWs in FP
 742 correspond to that obtained by looking at the most extreme events over the region in the global-scale study of Marin et al.,
 743 (2022) (their Fig. 3 and 4). RES-MHWs, which are predominant in the equatorial region north of 2°S, have been mainly
 744 attributed to anomalous vertical mixing processes that warm the mixed layer during the onset and decay phases (Bian et al.,
 745 2023). Further south, over FP, the residual contributions observed during onset and decay in our analysis (Fig. A1, A2) have
 746 not been explored in detail in this study because the amplitude of the data assimilation increments is unknown. Nevertheless,
 747 as stated in our study this residual may partly reflect the effect of weakened winds during MHW onset and decay (Fig. 9)
 748 that are favored by EN (in the northeast) and LN (in the southwest), which can reduce vertical heat transfer through diffusion
 749 and local mixing (Vogt et al., 2022). It has also been shown that mesoscale eddies can inhibit the vertical mixing driven by
 750 internal waves over the region, limiting subsurface cooling and thereby promoting the development of extreme subsurface



a supprimé:

a supprimé: Conclusion

The present study provides a comprehensive assessment of MHWs in the south central Pacific across FP, characterizing their spatial and seasonal variability, mechanisms, and modulation by ENSO and its various flavors. MHWs were analyzed using OISST data for the 1981–2024 period, as well as with the GLORYS reanalysis for 1993–2024. GLORYS agreement with OISST gave us confidence in the ability of the reanalysis to study MHW mechanisms over 1993–2020. Hence, by examining the mixed layer heat budget during MHWs in GLORYS, we could determine the main mechanisms at work during MHW intensification and decay phases. We showed that MHW occurrence, intensity, and duration vary significantly between archipelagos and seasons. The Marquesas and Austral Islands experienced the highest number of MHW days during the warm season, as well as the most intense and long-lasting events. In contrast, the Society, Tuamotu, and Gambier Islands tend to experience MHWs of lower intensity and duration, particularly during the cold season. Cumulative intensity and duration extremes also varied spatially, reflecting region-specific mechanisms. Our results highlight the dominant role of air–sea fluxes in driving MHWs in the central regions (Society–Tuamotu–Gambier), while oceanic advection is the key mechanism generating MHWs in the Marquesas and equatorward zones up to 2°S where vertical processes dominate. In the Austral Islands and poleward zones, both air–sea fluxes and horizontal advection contribute comparably. During the cold season, the role of horizontal advection becomes more prominent across FP, while the impact of surface fluxes is da ... [12]

a supprimé: categories

a supprimé: (

a mis en forme : Anglais (E.U.)

a supprimé:

824 temperatures (Wyatt et al., 2023). Tides—and therefore internal tides—are not explicitly represented in GLORYS, and FP is
825 a major internal-tide generation region (Zaron, 2019). The substantial number of RES-MHWs detected over FP (Fig. 6c,g)
826 therefore highlights the need for regional modeling that resolves tidal processes.
827 One limitation of our study is [its](#) focus on [surface temperatures](#), whereas extreme temperatures can also occur throughout the
828 water column [with](#) severe impacts on ecosystems (Wyatt et al., 2023) — either synchronously with the surface, more intense,
829 less intense, or even entirely decoupled from surface extremes (Zhang et al., 2023). The mechanisms driving these
830 subsurface extremes may differ from those at the surface revealed in this work, due to the vertical structure of ocean currents
831 in the region and the progressive attenuation of air–sea flux influences with depth. Our analysis gives confidence in
832 GLORYS, to study vertical extent of MHW. Lal et al. (2025) showed that surface MHWs in the extreme western part of FP
833 are generally confined to the seasonal mixed layer north of 20°S, but extend deeper south of this latitude, providing an
834 indication of what might be expected for the vertical extent of MHWs detected over FP in this study.
835 We showed that ENSO provided favorable or unfavorable background conditions for MHW development during the warm
836 season and to a lesser extent over the austral winter, depending on the region within FP and the ENSO phase. However,
837 except in the extreme northern regions, including the Marquesas during extreme EPEN and strong MEN events—where the
838 surface ocean remains in a persistent MHW state throughout the whole warm season—the actual triggers of the mechanisms
839 creating MHW onset (extreme LHF and SW anomalies) remain to be fully understood. Intra-seasonal processes such as the
840 Madden–Julian Oscillation (MJO), equatorial wave activity, and/or stochastic weather/oceanic events ([Tropical Cyclones](#),
841 prolonged periods of high/ weak surface winds, prolonged precipitation/clear sky periods, SPCZ intra-seasonal variability,
842 oceanic eddies) may initiate or terminate MHWs. In this context, ENSO primarily modulated the background state,
843 influencing how these intra-seasonal triggers affect MHW development and persistence (MJO-ENSO compound events as an
844 example, Dutheil et al., 2024). Further work is needed to understand how ENSO and these higher frequency variations
845 interact together.
846 Our work builds on ongoing efforts to understand the characteristics and mechanisms of MHWs across South Pacific
847 countries ([Holbrook et al., 2022](#), Dutheil et al., 2024; Lal et al., 2025). MHWs display distinct features between the western
848 and central South Pacific, underscoring the need for such regional analyses. Even within the FP region, while we present
849 results at the archipelago scale, notable variability [was](#) found within the Tuamotu archipelago itself, which spans from about
850 10°N to 23°S (Fig. 3e).
851 Many of the FP islands (except in the Marquesas) are fringed by reefs that enclose lagoons, which most of the time represent
852 a key economic resource for local communities. MHWs can have devastating impacts on such ecosystems (Glynn, 1984;
853 Mumby et al., 2001b; Andréfouët et al., 2015; Andréfouët and Adjeroud, 2019; Hédouin et al., 2020). These lagoons exhibit
854 diverse geomorphological characteristics, such as differences in size and degree of openness to the open ocean, making it
855 challenging to assess how large-scale oceanic MHWs propagate into these more sheltered environments. To achieve this at
856 the atoll and lagoon scale, this requires validating high-resolution satellite SST products against in-situ observations (e.g.,
857 ReefTemp; Van Wynsberge et al., 2017; Le Gendre et al., 2024), alongside a detailed understanding of lagoon

a supprimé: A regional ocean model such as the Coastal and Regional Ocean Community model (CROCO, , with explicit tidal forcing, would help better quantifying the residual contributions to MHWs development and decay....

a supprimé: the

a supprimé: SST

a supprimé: and cause

a supprimé: TCs

a supprimé: .

a supprimé: has been

868 hydrodynamics (Bruyère et al., 2023). Additionally, the development of hydrodynamical or statistical models that relate
869 lagoon interior surface temperatures to oceanic temperatures and ocean–meteorological conditions could help compensate
870 for the current lack of high-resolution SST data (Van Wynsberge et al., 2017, 2024).

871 In Fig. 5 we related ENSO flavors to DHW, the NOAA metric used to monitor coral bleaching globally. NOAA’s historical
872 alert levels are: 0–4 (possible bleaching), 4–8 (reef-wide bleaching risk), and >8 (reef-wide bleaching with potential
873 mortality). In our record, the 8 threshold is rarely reached in the Society and Tuamotu—even in 2015/16 (Fig. 5; Fig. S11),
874 when widespread bleaching was documented (Hédouin et al., 2020). This underscores known limitations of the standard
875 DHW formulation, which can underpredict bleaching and overlooks regional sensitivities. It has been shown that tuning the
876 hotspot definition, accumulation window, and/or bleaching threshold improves coral bleaching forecast skill (e.g. Lachs et
877 al., 2021; Whitaker and DeCarlo, 2024), but that these adjustments often become region- or location-specific, rendering
878 generalization difficult. Accordingly, Fig. 5 quantitative results should not be read as direct indicator of coral bleaching;
879 rather, it shows how ENSO modulates cumulative heat stress across FP’s archipelagos. Bleaching occurrence is also
880 modulated by other environmental factors than heat stress—e.g., UV-exposition, the shortwave radiation reaching colonies at
881 depth, salinity, water depth, nutrient supply, and local hydrodynamics (DeCarlo et al., 2020; Gonzalez-Espinosa and Donner,
882 2021). As an example, over FP increased cloud cover has been suspected to spare Society Islands from massive coral
883 bleaching in the extreme EPEN 1997/98 event (Mumby et al., 2001).

884 While the OISST dataset has been shown to be well-suited for the analysis carried out in this study (Gupta and Sil 2024),
885 differences between SST products can be significant for some commonly used MHW metrics (Chevallard et al., 2025) and
886 this should be kept in mind. For analyzing ENSO modulation, products generally yield consistent patterns (here OISST and
887 GLORYS are coherent). However, at the archipelago scale, quantitative metrics can differ between products (Fig. S7).

888 Our results provide crucial insights into the mechanisms driving MHWs over FP and their link with ENSO, which are
889 essential for improving seasonal-to-interannual forecasts of these extreme events. The forecasting skill of MHWs varies
890 significantly depending on season, region, and lead time (de Boissésou and Balmaseda, 2024; Cohen et al., 2025; Jacox et
891 al., 2022). In particular, there is a strong ENSO imprint on the predictability of these events. Over the northeastern region of
892 FP, MHWs appear much more predictable than in southern regions, with minimal forecast skill in the central areas where
893 MHWs are primarily controlled by air–sea fluxes (Fig. 6). In the southwestern part of FP, MHW forecast skill is also weak,
894 likely due to the dominant influence of horizontal advection (HADV) and mesoscale circulation features during the MHW
895 onset and decay. These findings point to the need for higher-resolution models, along with an expanded network of ocean
896 observations, to improve verification of the models and forecasting capabilities in this region.

897 Across the entire FP region, both the number of MHW days and event durations have increased over time (Fig. S20).
898 However, maximum intensity has increased only in the southwestern half of the country—including the Society
899 Archipelago, southern Tuamotu, Gambier, and Austral Islands—while the northern Tuamotu and Marquesas have
900 experienced a decrease in maximum MHW intensity over time (Fig. S20b). The spatial pattern of this trend closely mirrors
901 that of the long-term SST trend across the region (see Fig. S1). The underlying cause of this cooling trend in the northeast

a mis en forme : Anglais (E.U.)

a supprimé :

a supprimé : directly as relating the presence

a mis en forme : Anglais (G.B.)

a mis en forme : Anglais (E.U.)

a mis en forme : Anglais (E.U.)

a supprimé : spread

a supprimé : MHWs

a mis en forme : Anglais (E.U.)

906 which extends more broadly in the eastern tropical Pacific remains to be clarified—whether it reflects the influence of global
907 warming, natural tropical Pacific decadal variability, or more likely a combination of both (Watanabe et al., 2024).
908 Therefore, the observed cooling trend in MHWs intensity over the northeastern region needs to be interpreted carefully.
909

910 7- Conclusion

911 The present study provides a comprehensive assessment of MHWs in the south central Pacific across FP, characterizing their
912 spatial and seasonal variability, mechanisms, and modulation by ENSO and its various flavors. MHWs were analyzed using
913 OISST data for the 1981–2024 period, as well as with the GLORYS reanalysis for 1993–2024. GLORYS agreement with
914 OISST gave us confidence in the ability of the reanalysis to study MHW mechanisms over 1993–2020. Hence, by examining
915 the mixed layer heat budget during MHWs in GLORYS, we were able to determine the main mechanisms at work during
916 MHW intensification and decay phases.

917 We showed that MHW occurrence, intensity, and duration vary significantly between archipelagos and seasons. The
918 Marquesas and Austral Islands experienced the highest number of MHW days during the warm season, as well as the most
919 intense and long-lasting events. In contrast, the Society, Tuamotu, and Gambier Islands tend to experience MHWs of lower
920 intensity and duration, particularly during the cold season. Cumulative intensity and duration extremes also varied spatially,
921 reflecting region-specific mechanisms.

922 Our results highlight the dominant role of air–sea fluxes in driving MHWs in the central regions (Society–Tuamotu–
923 Gambier), while oceanic advection is the key mechanism generating MHWs in the Marquesas and equatorward zones up to
924 2°S where vertical processes dominate. In the Austral Islands and poleward zones, both air-sea fluxes and horizontal
925 advection contribute comparably. During the cold season, the role of horizontal advection becomes more prominent across
926 FP, while the impact of surface fluxes is dampened by a deeper seasonal mixed layer. Generally, most of MHWs decay is
927 driven by air-sea fluxes.

928 We also demonstrated that ENSO exerts a strong and spatially structured modulation on MHWs in FP. EN favors MHW
929 development in the northeastern region (Marquesas–northern Tuamotu), while LN promotes MHWs in the southwest
930 (Austral Islands). These effects are linked to seasonally persistent changes in SST, surface wind speed, MLD, and oceanic
931 horizontal advection patterns.

932 This work provides new insights into the processes controlling MHWs across FP and their connection to large-scale climate
933 variability. It also offers a framework for understanding how future changes in ENSO behavior and ocean–atmosphere
934 coupling might influence the frequency and severity of MHWs over the region.

935

936

937 *Authors contribution*

938 BP, TI and SC designed the study and wrote the initial manuscript draft. BP performed the analysis presented in this
939 manuscript. Discussions and iterative feedback from all co-authors significantly contributed to the revision of the
940 manuscript.

941

942 *Competing interests*

943 The authors declare that they have no conflict of interest.

944

945 *Acknowledgments*

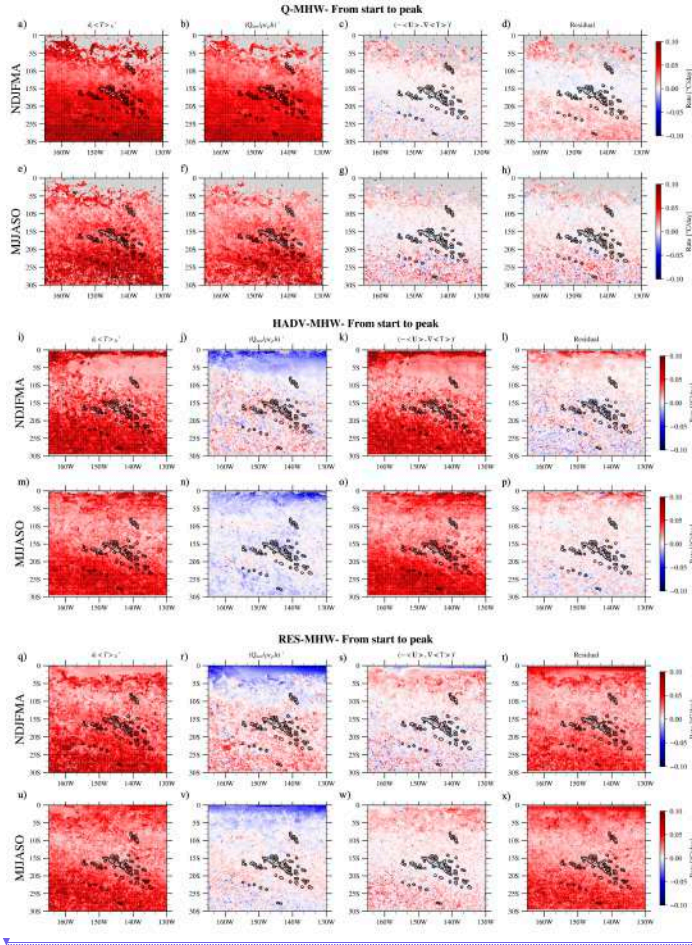
946 B. P. is supported by the Institut de Recherche pour le Développement (IRD) through IRD PhD funding and is hosted at the
947 UMR 241 SECOPOL laboratory at UPF. [B. P and A. B. also acknowledge SPC \(Pacific Community\) funding through their](#)
948 [climate flagship programs](#). The author acknowledge the support of the French Agence Nationale de la Recherche (ANR), as
949 part of the France 2030 program, under grant ANR-23-POCE-0001 (project MaHeWa), and of the Fonds Pacifique (project
950 HEAT). We acknowledge the use of Python and NOAA Pyfer- ret languages and of the several data servers listed below.

951

952 *Data Availability Statement*

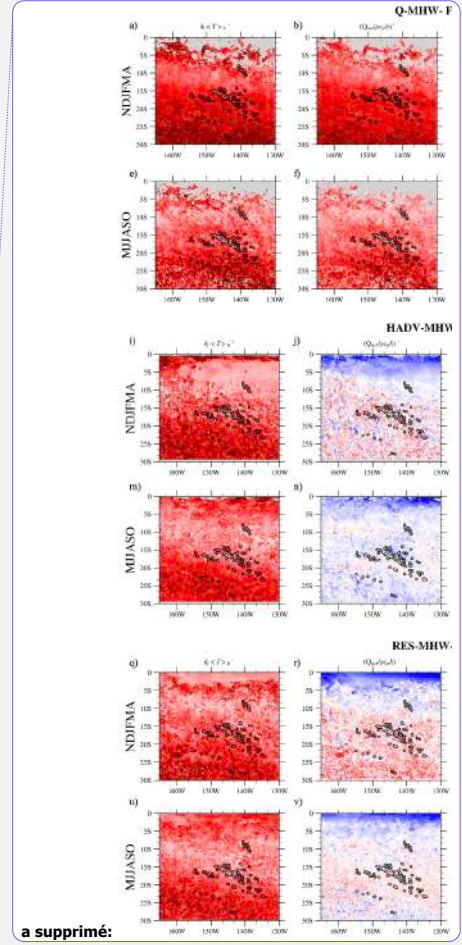
953 All datasets used in this study are open source and available online. The OISSTv2 data were downloaded from
954 <https://psl.noaa.gov/data/gridded/data.noaa.oisst.v2.highres.html>. The GLORYS reanalysis is available on Copernicus
955 https://data.marine.copernicus.eu/product/GLOBAL_MULTIYEAR_PHY_001_030/description. The official administrative
956 geographic dataset used for delimitating the archipelagos of French Polynesia are available
957 at <https://www.data.gouv.fr/fr/datasets/geographie-administrative-de-la-polynesie-francaise/>. All scripts used to obtain the
958 results presented in this study were written in Python and Pyferret and can be shared upon request.

959

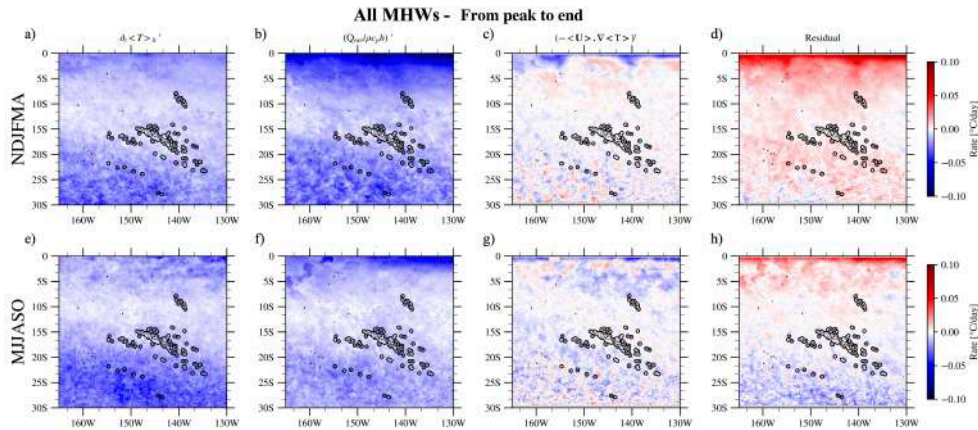


961

962 **Figure A1.** Composites across all events at each grid point of the different term of the heat budget analysis Eq. (2) averaged from start to
 963 peak for each MHW type and for each season separately. The first column corresponds to the mixed-layer temperature tendency term, the
 964 second one corresponds to air/sea flux heat budget term, the third one corresponds to the horizontal heat advection term and the fourth one
 965 corresponds to the residual term. They are all expressed in °C/day. Panels a–d and e–h show composites of Q-MHWs during austral
 966 summer and winter, respectively. Panels i–l and m–p show composites of HADV-MHWs for summer and winter, respectively. Panels q–t
 967 and u–x present composites of RES-MHWs in austral summer and winter, respectively.



a supprimé:



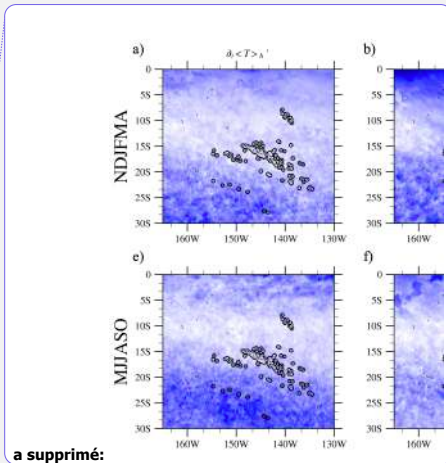
969

970 **Figure A2.** Composites across all events at each grid point of the different term of the heat budget analysis Eq. (2) averaged from peak to
 971 end for all MHWs and for each season separately. The first column corresponds to the mixed-layer temperature tendency term, the second
 972 corresponds to air/sea flux heat budget term, the third one corresponds to the horizontal heat advection term and the fourth one
 973 corresponds to the residual term. They are all expressed in °C/day. Panels a-d and e-h show the composite over MHWs in austral summer
 974 and winter respectively.

975

976 References

- 977 Amaya, D. J., Jacox, M. G., Fewings, M. R., Saba, V. S., Stuecker, M. F., Rykaczewski, R. R., Ross, A. C., Stock, C. A.,
 978 Capotondi, A., Petrik, C. M., Bograd, S. J., Alexander, M. A., Cheng, W., Hermann, A. J., Kearney, K. A., and Powell, B.
 979 S.: Marine heatwaves need clear definitions so coastal communities can adapt, *Nature*, 616, 29–32,
 980 <https://doi.org/10.1038/d41586-023-00924-2>, 2023.
 981 Andréfouët, S. and Adjeroud, M.: French Polynesia, in: *World Seas: an Environmental Evaluation*, Elsevier, 827–854,
 982 <https://doi.org/10.1016/B978-0-08-100853-9.00039-7>, 2019.
 983 Andréfouët, S., Dutheil, C., Menkes, C. E., Bador, M., and Lengaigne, M.: Mass mortality events in atoll lagoons:
 984 environmental control and increased future vulnerability, *Glob. Change Biol.*, 21, 195–205,
 985 <https://doi.org/10.1111/gcb.12699>, 2015.
 986 Bian, C., Jing, Z., Wang, H., Wu, L., Chen, Z., Gan, B., and Yang, H.: Oceanic mesoscale eddies as crucial drivers of global
 987 marine heatwaves, *Nat. Commun.*, 14, 2970, <https://doi.org/10.1038/s41467-023-38811-z>, 2023.
 988 Bian, C., Jing, Z., Wang, H., and Wu, L.: Scale-Dependent Drivers of Marine Heatwaves Globally, *Geophys. Res. Lett.*, 51,



a supprimé:

990 e2023GL107306, <https://doi.org/10.1029/2023GL107306>, 2024.

991 de Boissésou, E. and Balmaseda, M. A.: Predictability of marine heatwaves: assessment based on the ECMWF seasonal
992 forecast system, *Ocean Sci.*, 20, 265–278, <https://doi.org/10.5194/os-20-265-2024>, 2024.

993 Bretherton, C. S., Widmann, M., Dymnikov, V. P., Wallace, J. M., and Bladé, I.: The Effective Number of Spatial Degrees
994 of Freedom of a Time-Varying Field, *J. Clim.*, 12, 1990–2009, [https://doi.org/10.1175/1520-995-0442\(1999\)012<1990:TENOSD>2.0.CO;2](https://doi.org/10.1175/1520-995-0442(1999)012<1990:TENOSD>2.0.CO;2), 1999.

996 Bruyère, O., Le Gendre, R., Chauveau, M., Bourgeois, B., Varillon, D., Butscher, J., Trophime, T., Follin, Y., Aucan, J.,
997 Liao, V., and Andréfouët, S.: Lagoon hydrodynamics of pearl farming atolls: the case of Raroia, Takapoto, Apataki and
998 Takarua (French Polynesia), *Earth Syst. Sci. Data*, 15, 5553–5573, <https://doi.org/10.5194/essd-15-5553-2023>, 2023.

999 Capotondi, A., Wittenberg, A. T., Kug, J.-S., Takahashi, K., and McPhaden, M. J.: ENSO Diversity, in: El Niño Southern
1000 Oscillation in a Changing Climate, American Geophysical Union (AGU), 65–86,
1001 <https://doi.org/10.1002/9781119548164.ch4>, 2020.

1002 Capotondi, A., Rodrigues, R. R., Sen Gupta, A., Benthuisen, J. A., Deser, C., Frölicher, T. L., Lovenduski, N. S., Amaya, D.
1003 J., Le Grix, N., Xu, T., Hermes, J., Holbrook, N. J., Martínez-Villalobos, C., Masina, S., Roxy, M. K., Schaeffer, A.,
1004 Schlegel, R. W., Smith, K. E., and Wang, C.: A global overview of marine heatwaves in a changing climate, *Commun. Earth*
1005 *Environ.*, 5, 701, <https://doi.org/10.1038/s43247-024-01806-9>, 2024.

1006 Chevillard, C., Le Gendre, R., Menkes, C., Izumo, T., Pagli, B., Van Wynsberge, S., and Cravatte, S.: Sensitivity of marine
1007 heatwaves metrics to SST products, focusing on the Tropical Pacific, *EGUsphere*, 1–36, <https://doi.org/10.5194/egusphere-1008-2025-5417>, 2025.

1009 Cohen, J. T., Thompson, L., Maroon, E., Deppenmeier, A.-L., and Cai, C.: Object-Based Evaluation of Seasonal-to-
1010 Multiyear Marine Heatwave Predictions, *Geophys. Res. Lett.*, 52, e2025GL115021, <https://doi.org/10.1029/2025GL115021>,
1011 2025.

1012 datagouv. *Géographie administrative de la Polynésie française*. Available
1013 at: <https://www.data.gouv.fr/fr/datasets/geographie-administrative-de-la-polynesie-francaise/> (last access: April 2025).

1014 DeCarlo, T. M., Gajdzik, L., Ellis, J., Coker, D. J., Roberts, M. B., Hammerman, N. M., Pandolfi, J. M., Monroe, A. A., and
1015 Berumen, M. L.: Nutrient-supplying ocean currents modulate coral bleaching susceptibility, *Sci. Adv.*, 6, eabc5493,
1016 <https://doi.org/10.1126/sciadv.abc5493>, 2020.

1017 Dee, D. P., Uppala, S. M., Simmons, A. J., Berrisford, P., Poli, P., Kobayashi, S., Andrae, U., Balmaseda, M. A., Balsamo,
1018 G., Bauer, P., Bechtold, P., Beljaars, A. C. M., Van De Berg, L., Bidlot, J., Bormann, N., Delsol, C., Dragani, R., Fuentes,
1019 M., Geer, A. J., Haimberger, L., Healy, S. B., Hersbach, H., Hólm, E. V., Isaksen, L., Kållberg, P., Köhler, M., Matricardi,
1020 M., McNally, A. P., Monge-Sanz, B. M., Morcrette, J. -J., Park, B. -K., Peubey, C., De Rosnay, P., Tavolato, C., Thépaut, J.
1021 -N., and Vitart, F.: The ERA-Interim reanalysis: configuration and performance of the data assimilation system, *Q. J. R.*
1022 *Meteorol. Soc.*, 137, 553–597, <https://doi.org/10.1002/qj.828>, 2011.

1023 Deppenmeier, A.-L., Bryan, F. O., Kessler, W. S., and Thompson, L.: Modulation of Cross-Isothermal Velocities with

1024 ENSO in the Tropical Pacific Cold Tongue, *J. Phys. Oceanogr.*, 51, 1559–1574, <https://doi.org/10.1175/JPO-D-20-0217.1>,
1025 2021.

1026 Dutheil, C., Lal, S., Lengaigne, M., Cravatte, S., Menkès, C., Receveur, A., Börgel, F., Gröger, M., Houlbreque, F., Le
1027 Gendre, R., Mangolte, I., Peltier, A., and Meier, H. E. M.: The massive 2016 marine heatwave in the Southwest Pacific: An
1028 “El Niño–Madden-Julian Oscillation” compound event, *Sci. Adv.*, 10, eadp2948, <https://doi.org/10.1126/sciadv.adp2948>,
1029 2024.

1030 Elzahaby, Y., Schaeffer, A., Roughan, M., and Delaux, S.: Oceanic Circulation Drives the Deepest and Longest Marine
1031 Heatwaves in the East Australian Current System, *Geophys. Res. Lett.*, 48, e2021GL094785,
1032 <https://doi.org/10.1029/2021GL094785>, 2021.

1033 Elzahaby, Y., Schaeffer, A., Roughan, M., and Delaux, S.: Why the Mixed Layer Depth Matters When Diagnosing Marine
1034 Heatwave Drivers Using a Heat Budget Approach, *Front. Clim.*, 4, <https://doi.org/10.3389/fclim.2022.838017>, 2022.

1035 Glynn, P. W.: Widespread Coral Mortality and the 1982–83 El Niño Warming Event, *Environ. Conserv.*, 11, 133–146,
1036 <https://doi.org/10.1017/S0376892900013825>, 1984.

1037 Gonzalez-Espinosa, P. C. and Donner, S. D.: Cloudiness reduces the bleaching response of coral reefs exposed to heat stress,
1038 *Glob. Change Biol.*, 27, 3474–3486, <https://doi.org/10.1111/gcb.15676>, 2021.

1039 Gregory, C. H., Artana, C., Lama, S., León-FonFay, D., Sala, J., Xiao, F., Xu, T., Capotondi, A., Martinez-Villalobos, C.,
1040 and Holbrook, N. J.: Global Marine Heatwaves Under Different Flavors of ENSO, *Geophys. Res. Lett.*, 51,
1041 e2024GL110399, <https://doi.org/10.1029/2024GL110399>, 2024.

1042 Gupta, H. and Sil, S.: Assessment of GHRSSST and OISST Datasets in Identification of Marine Heat-Waves and Heat-
1043 Spikes, *IEEE Geosci. Remote Sens. Lett.*, 21, 1–5, <https://doi.org/10.1109/LGRS.2024.3362474>, 2024.

1044 Hédouin, L., Rouzé, H., Berthe, C., Perez-Rosales, G., Martínez, E., Chancerelle, Y., Galand, P. E., Lerouvreur, F., Nugues,
1045 M. M., Pochon, X., Siu, G., Steneck, R., and Planes, S.: Contrasting patterns of mortality in Polynesian coral reefs following
1046 the third global coral bleaching event in 2016, *Coral Reefs*, 39, 939–952, <https://doi.org/10.1007/s00338-020-01914-w>,
1047 2020.

1048 Hersbach, H., Bell, B., Berrisford, P., Hirahara, S., Horányi, A., Muñoz-Sabater, J., Nicolas, J., Peubey, C., Radu, R.,
1049 Schepers, D., Simmons, A., Soci, C., Abdalla, S., Abellan, X., Balsamo, G., Bechtold, P., Biavati, G., Bidlot, J., Bonavita,
1050 M., De Chiara, G., Dahlgren, P., Dee, D., Diamantakis, M., Dragani, R., Flemming, J., Forbes, R., Fuentes, M., Geer, A.,
1051 Haimberger, L., Healy, S., Hogan, R. J., Hólm, E., Janisková, M., Keeley, S., Laloyaux, P., Lopez, P., Lupu, C., Radnoti, G.,
1052 de Rosnay, P., Rozum, I., Vamborg, F., Villaume, S., and Thépaut, J.-N.: The ERA5 global reanalysis, *Q. J. R. Meteorol.*
1053 *Soc.*, 146, 1999–2049, <https://doi.org/10.1002/qj.3803>, 2020.

1054 Hobday, A. J., Alexander, L. V., Perkins, S. E., Smale, D. A., Straub, S. C., Oliver, E. C. J., Benthuisen, J. A., Burrows, M.
1055 T., Donat, M. G., Feng, M., Holbrook, N. J., Moore, P. J., Scannell, H. A., Sen Gupta, A., and Wernberg, T.: A hierarchical
1056 approach to defining marine heatwaves, *Prog. Oceanogr.*, 141, 227–238, <https://doi.org/10.1016/j.pocean.2015.12.014>, 2016.

1057 Hobday, A. J., Oliver, E. C. J., Gupta, A. S., Benthuisen, J. A., Burrows, M. T., Donat, M. G., Holbrook, N. J., Moore, P. J.,

1058 Thomsen, M. S., Wernberg, T., and Smale, D. A.: Categorizing and Naming MARINE HEATWAVES, *Oceanography*, 31,
1059 162–173, 2018.

1060 Holbrook, N., Sen Gupta, A., Oliver, E., Hobday, A., Benthuyesen, J., Scannell, H., Smale, D., and Wernberg, T.: Keeping
1061 pace with marine heatwaves, *Nat. Rev. Earth Environ.*, 1, <https://doi.org/10.1038/s43017-020-0068-4>, 2020.

1062 Holbrook, N. J., Scannell, H. A., Sen Gupta, A., Benthuyesen, J. A., Feng, M., Oliver, E. C. J., Alexander, L. V., Burrows, M.
1063 T., Donat, M. G., Hobday, A. J., Moore, P. J., Perkins-Kirkpatrick, S. E., Smale, D. A., Straub, S. C., and Wernberg, T.: A
1064 global assessment of marine heatwaves and their drivers, *Nat. Commun.*, 10, 2624, <https://doi.org/10.1038/s41467-019-10206-z>, 2019.

1066 Holbrook, N. J., Hernaman, V., Koshiba, S., Lako, J., Kajtar, J. B., Aмоса, P., and Singh, A.: Impacts of marine heatwaves
1067 on tropical western and central Pacific Island nations and their communities, *Glob. Planet. Change*, 208, 103680,
1068 <https://doi.org/10.1016/j.gloplacha.2021.103680>, 2022.

1069 Huang, B., Liu, C., Banzon, V., Freeman, E., Graham, G., Hankins, B., Smith, T., and Zhang, H.-M.: Improvements of the
1070 Daily Optimum Interpolation Sea Surface Temperature (DOISST) Version 2.1, *J. Clim.*, 34, 2923–2939,
1071 <https://doi.org/10.1175/JCLI-D-20-0166.1>, 2021.

1072 Jacox, M. G., Alexander, M. A., Amaya, D., Becker, E., Bograd, S. J., Brodie, S., Hazen, E. L., Pozo Buil, M., and
1073 Tommasi, D.: Global seasonal forecasts of marine heatwaves, *Nature*, 604, 486–490, <https://doi.org/10.1038/s41586-022-1074-04573-9>, 2022.

1075 Lachs, L., Bythell, J. C., East, H. K., Edwards, A. J., Mumby, P. J., Skirving, W. J., Spady, B. L., and Guest, J. R.: Fine-
1076 Tuning Heat Stress Algorithms to Optimise Global Predictions of Mass Coral Bleaching, *Remote Sens.*, 13, 2677,
1077 <https://doi.org/10.3390/rs13142677>, 2021.

1078 Lal, S., Cravatte, S., Menkes, C., Macdonald, J., LeGendre, R., Mangolte, I., Dutheil, C., Holbrook, N., and Nicol, S.:
1079 Characterization of Past Marine Heatwaves around South Pacific Island Countries: What really matters?, *EGUsphere*, 1–48,
1080 <https://doi.org/10.5194/egusphere-2025-3281>, 2025.

1081 Le Gendre, R., Varillon, D., Fiat, S., Hocdé, R., De Ramon N’Yeurt, A., Aucan, J., Cravatte, S., Duphil, M., Ganachaud, A.,
1082 Gaudron, B., Kestenare, E., Liao, V., Pelletier, B., Peltier, A., Schaefer, A.-L., Trophime, T., Van Wynsberge, S.,
1083 Dandonneau, Y., Allenbach, M., and Menkes, C.: ReefTEMPs: The Pacific Islands Coastal Temperature Network, *Earth*
1084 *Syst. Sci. Data Discuss.*, 1–41, <https://doi.org/10.5194/essd-2024-394>, 2024.

1085 Lellouche, J.-M., Greiner, E., Le Galloudec, O., Garric, G., Regnier, C., Drévilion, M., Benkiran, M., Testut, C.-E.,
1086 Bourdalle-Badie, R., Gasparin, F., Hernandez, O., Levier, B., Drillet, Y., Remy, E., and Le Traon, P.-Y.: Recent updates to
1087 the Copernicus Marine Service global ocean monitoring and forecasting real-time 1/12° high-resolution system, *Ocean Sci.*,
1088 14, 1093–1126, <https://doi.org/10.5194/os-14-1093-2018>, 2018.

1089 Lellouche, J.-M., Greiner, E., Bourdallé-Badie, R., Garric, G., Melet, A., Drévilion, M., Bricaud, C., Hamon, M., Le
1090 Galloudec, O., Regnier, C., Candela, T., Testut, C.-E., Gasparin, F., Ruggiero, G., Benkiran, M., Drillet, Y., Le Traon, P.-Y.,
1091 Bourdallé-Badie, R., Garric, G., Melet, A., Drévilion, M., Bricaud, C., Hamon, M., Le Galloudec, O., Regnier, C., Candela,

1092 T., Testut, C.-E., Gasparin, F., Ruggiero, G., Benkiran, M., Drillet, Y., and Le Traon, P.-Y.: The Copernicus Global 1/12°
1093 Oceanic and Sea Ice GLORYS12 Reanalysis, *Front. Earth Sci.*, 9, <https://doi.org/10.3389/feart.2021.698876>, 2021.

1094 Madec, G., Bell, M., Benshila, R., Blaker, A., Boudrallé-Badie, R., Bricaud, C., Bruciaferri, D., Carneiro, D., Castrillo, M.,
1095 Calvert, D., Chanut, J., Clementi, E., Coward, A., Laverigne, C. de, Dobricic, S., Epicoco, I., Éthé, C., Fiedler, E., Ford, D.,
1096 Furner, R., Ganderton, J., Graham, T., Harle, J., Hutchinson, K., Iovino, D., King, R., Lea, D., Levy, C., Lovato, T.,
1097 Maisonnave, E., Mak, J., Sanchez, J. M. C., Martin, M., Martin, N., Martins, D., Masson, S., Mathiot, P., Mele, F.,
1098 Mocavero, S., Moulin, A., Müller, S., Nursler, G., Oddo, P., Paronuzzi, S., Paul, J., Peltier, M., Person, R., Rousset, C.,
1099 Rynders, S., Samson, G., Schroeder, D., Storkey, D., Storto, A., Téchené, S., Vancoppenolle, M., and Wilson, C.: NEMO
1100 Ocean Engine Reference Manual, <https://doi.org/10.5281/zenodo.14515373>, 2024.

1101 Marin, M., Feng, M., Bindoff, N. L., and Phillips, H. E.: Local Drivers of Extreme Upper Ocean Marine Heatwaves
1102 Assessed Using a Global Ocean Circulation Model, *Front. Clim.*, 4, <https://doi.org/10.3389/fclim.2022.788390>, 2022.

1103 Martinez, E., Ganachaud, A., Lefevre, J., and Maamaatuaiahutapu, K.: Central South Pacific thermocline water circulation
1104 from a high-resolution ocean model validated against satellite data: Seasonal variability and El Niño 1997–1998 influence, *J.*
1105 *Geophys. Res. Oceans*, 114, <https://doi.org/10.1029/2008JC004824>, 2009.

1106 Moisan, J. R. and Niiler, P. P.: The Seasonal Heat Budget of the North Pacific: Net Heat Flux and Heat Storage Rates (1950–
1107 1990), *J. Phys. Oceanogr.*, 28, 401–421, [https://doi.org/10.1175/1520-0485\(1998\)028<0401:TSHBOT>2.0.CO;2](https://doi.org/10.1175/1520-0485(1998)028<0401:TSHBOT>2.0.CO;2), 1998.

1108 Mumby, P., Chisholm, J., Edwards, A., Andrefouet, S., and Jaubert, J.: Cloudy weather may have saved Society Island reef
1109 corals during the 1998 ENSO event, *Mar. Ecol. Prog. Ser.*, 222, 209–216, <https://doi.org/10.3354/meps222209>, 2001a.

1110 Mumby, P., Chisholm, J., Edwards, A., Clark, C., Roark, E., Andrefouet, S., and Jaubert, J.: Unprecedented bleaching-
1111 induced mortality in *Porites* spp. at Rangiroa Atoll, French Polynesia, *Mar. Biol.*, 139, 183–189,
1112 <https://doi.org/10.1007/s002270100575>, 2001b.

1113 Oliver, E. C. J., Donat, M. G., Burrows, M. T., Moore, P. J., Smale, D. A., Alexander, L. V., Benthuisen, J. A., Feng, M.,
1114 Sen Gupta, A., Hobday, A. J., Holbrook, N. J., Perkins-Kirkpatrick, S. E., Scannell, H. A., Straub, S. C., and Wernberg, T.:
1115 Longer and more frequent marine heatwaves over the past century, *Nat. Commun.*, 9, 1324, [https://doi.org/10.1038/s41467-](https://doi.org/10.1038/s41467-018-03732-9)
1116 018-03732-9, 2018.

1117 Oliver, E. C. J., Burrows, M. T., Donat, M. G., Sen Gupta, A., Alexander, L. V., Perkins-Kirkpatrick, S. E., Benthuisen, J.
1118 A., Hobday, A. J., Holbrook, N. J., Moore, P. J., Thomsen, M. S., Wernberg, T., and Smale, D. A.: Projected Marine
1119 Heatwaves in the 21st Century and the Potential for Ecological Impact, *Front. Mar. Sci.*, 6, 2019.

1120 Oliver, E. C. J., Benthuisen, J. A., Darmaraki, S., Donat, M. G., Hobday, A. J., Holbrook, N. J., Schlegel, R. W., and Gupta,
1121 A. S.: Marine Heatwaves, *Annu. Rev. Mar. Sci.*, 13, 313–342, <https://doi.org/10.1146/annurev-marine-032720-095144>,
1122 2021.

1123 Pagli, B., Izumo, T., Cravatte, S. E., Hopuare, M., Martinoni-Lapierre, S., Laurent, V., Menkes, C., Monselesan, D., and
1124 Auffray, S.: The Diverse Impacts of El Niño and La Niña Events over the South Pacific and in French Polynesia, *J. Clim.*,
1125 38, 2681–2701, <https://doi.org/10.1175/JCLI-D-24-0408.1>, 2025.

1126 Paulson, C. A. and Simpson, J. J.: Irradiance Measurements in the Upper Ocean, *J. Phys. Oceanogr.*, 7, 952–956,
1127 [https://doi.org/10.1175/1520-0485\(1977\)007<0952:IMITUO>2.0.CO;2](https://doi.org/10.1175/1520-0485(1977)007<0952:IMITUO>2.0.CO;2), 1977.

1128 Pilo, G. S., Holbrook, N. J., Kiss, A. E., and Hogg, A. McC.: Sensitivity of Marine Heatwave Metrics to Ocean Model
1129 Resolution, *Geophys. Res. Lett.*, 46, 14604–14612, <https://doi.org/10.1029/2019GL084928>, 2019.

1130 Schlegel, R. W., Oliver, E. C. J., and Chen, K.: Drivers of Marine Heatwaves in the Northwest Atlantic: The Role of Air–Sea
1131 Interaction During Onset and Decline, *Front. Mar. Sci.*, 8, <https://doi.org/10.3389/fmars.2021.627970>, 2021.

1132 Sen Gupta, A.: Marine heatwaves: definition duel heats up, *Nature*, 617, 465–465, <https://doi.org/10.1038/d41586-023-01619-4>, 2023.

1134 Sen Gupta, A., Thomsen, M., Benthuisen, J. A., Hobday, A. J., Oliver, E., Alexander, L. V., Burrows, M. T., Donat, M. G.,
1135 Feng, M., Holbrook, N. J., Perkins-Kirkpatrick, S., Moore, P. J., Rodrigues, R. R., Scannell, H. A., Taschetto, A. S.,
1136 Ummenhofer, C. C., Wernberg, T., and Smale, D. A.: Drivers and impacts of the most extreme marine heatwave events, *Sci.*
1137 *Rep.*, 10, 19359, <https://doi.org/10.1038/s41598-020-75445-3>, 2020.

1138 Skirving, W., Marsh, B., De La Cour, J., Liu, G., Harris, A., Maturi, E., Geiger, E., and Eakin, C. M.: CoralTemp and the
1139 Coral Reef Watch Coral Bleaching Heat Stress Product Suite Version 3.1, *Remote Sens.*, 12, 3856,
1140 <https://doi.org/10.3390/rs12233856>, 2020.

1141 Smith, K. E., Sen Gupta, A., Amaya, D., Benthuisen, J. A., Burrows, M. T., Capotondi, A., Filbee-Dexter, K., Frölicher, T.
1142 L., Hobday, A. J., Holbrook, N. J., Malan, N., Moore, P. J., Oliver, E. C. J., Richaud, B., Salcedo-Castro, J., Smale, D. A.,
1143 Thomsen, M., and Wernberg, T.: Baseline matters: Challenges and implications of different marine heatwave baselines,
1144 *Prog. Oceanogr.*, 231, 103404, <https://doi.org/10.1016/j.pocean.2024.103404>, 2025.

1145 Stackhouse, P. W., Cox, S. J., Mikovitz, J. C., and Zhang, T.: GEWEX (Global Energy and Water Exchanges Project):
1146 Surface Radiation Budget (SRB) Release 4 Integrated Product (IP4) - Algorithm Theoretical Basis Document and
1147 Evaluation, 2021.

1148 Van Wynsberge, S., Menkes, C., Le Gendre, R., Passfield, T., and Andréfouët, S.: Are Sea Surface Temperature satellite
1149 measurements reliable proxies of lagoon temperature in the South Pacific?, *Estuar. Coast. Shelf Sci.*, 199, 117–124,
1150 <https://doi.org/10.1016/j.ecss.2017.09.033>, 2017.

1151 Van Wynsberge, S., Quéré, R., Andréfouët, S., Autret, E., and Le Gendre, R.: Spatial variability of temperature inside atoll
1152 lagoons assessed with Landsat-8 satellite imagery, *Remote Sens. Appl. Soc. Environ.*, 36, 101340,
1153 <https://doi.org/10.1016/j.rsase.2024.101340>, 2024.

1154 Vincent, E. M., Lengaigne, M., Menkes, C. E., Jourdain, N. C., Marchesiello, P., and Madec, G.: Interannual variability of
1155 the South Pacific Convergence Zone and implications for tropical cyclone genesis, *Clim. Dyn.*, 36, 1881–1896,
1156 <https://doi.org/10.1007/s00382-009-0716-3>, 2011.

1157 Vogt, L., Burger, F. A., Griffies, S. M., and Frölicher, T. L.: Local Drivers of Marine Heatwaves: A Global Analysis With an
1158 Earth System Model, *Front. Clim.*, 4, <https://doi.org/10.3389/fclim.2022.847995>, 2022.

1159 Watanabe, M., Kang, S. M., Collins, M., Hwang, Y.-T., McGregor, S., and Stuecker, M. F.: Possible shift in controls of the

1160 tropical Pacific surface warming pattern, *Nature*, 630, 315–324, <https://doi.org/10.1038/s41586-024-07452-7>, 2024.

1161 Whitaker, H. and DeCarlo, T.: Re(de)fining degree-heating week: coral bleaching variability necessitates regional and
1162 temporal optimization of global forecast model stress metrics, *Coral Reefs*, 43, 969–984, [https://doi.org/10.1007/s00338-](https://doi.org/10.1007/s00338-024-02512-w)
1163 024-02512-w, 2024.

1164 Wyatt, A. S. J., Leichter, J. J., Washburn, L., Kui, L., Edmunds, P. J., and Burgess, S. C.: Hidden heatwaves and severe coral
1165 bleaching linked to mesoscale eddies and thermocline dynamics, *Nat. Commun.*, 14, 25, [https://doi.org/10.1038/s41467-022-](https://doi.org/10.1038/s41467-022-35550-5)
1166 35550-5, 2023.

1167 Zaron, E. D.: Baroclinic Tidal Sea Level from Exact-Repeat Mission Altimetry, *J. Phys. Oceanogr.*, 49, 193–210,
1168 <https://doi.org/10.1175/JPO-D-18-0127.1>, 2019.

1169 Zhang, Y., Du, Y., Feng, M., and Hobday, A. J.: Vertical structures of marine heatwaves, *Nat. Commun.*, 14, 1–12,
1170 <https://doi.org/10.1038/s41467-023-42219-0>, 2023.

1171

Page 5 : [1] a supprimé Bastien PAGLI 09/02/2026 20:31:00

Page 5 : [2] a mis en forme Bastien PAGLI 09/02/2026 20:31:00

Anglais (G.B.)

Page 5 : [3] a mis en forme Bastien PAGLI 09/02/2026 20:31:00

Anglais (G.B.)

Page 5 : [4] a mis en forme Bastien PAGLI 09/02/2026 20:31:00

Anglais (G.B.)

Page 5 : [5] a mis en forme Bastien PAGLI 09/02/2026 20:31:00

Anglais (G.B.)

Page 5 : [6] a mis en forme Bastien PAGLI 09/02/2026 20:31:00

Anglais (G.B.)

Page 5 : [7] a mis en forme Bastien PAGLI 09/02/2026 20:31:00

Anglais (G.B.)

Page 5 : [8] a mis en forme Bastien PAGLI 09/02/2026 20:31:00

Anglais (G.B.)

Page 5 : [9] a mis en forme Bastien PAGLI 09/02/2026 20:31:00

Anglais (E.U.)

Page 5 : [10] a mis en forme Bastien PAGLI 09/02/2026 20:31:00

Anglais (G.B.)

Page 10 : [11] a mis en forme Bastien PAGLI 09/02/2026 20:31:00

Anglais (E.U.)

Page 10 : [11] a mis en forme Bastien PAGLI 09/02/2026 20:31:00

Anglais (E.U.)

Page 25 : [12] a supprimé Bastien PAGLI 09/02/2026 20:31:00